Fuel 427 (2027) 140103

Contents lists available at ScienceDirect

Fuel

journal homepage: www.elsevier.com/locate/fuel

Full Length Article

Dual-metal co-catalyst integrated graphitic carbon nitride for photocatalytic hydrogen evolution reaction

Suraj Gupta [a,b,*], Samar Batool [c], Marjeta Maček Kržmanc [a], Nina Daneu [a,b], Joyal Johny [a,b], Rohan Arya [d], Kishan H. Mali [d], Alpa Dashora [d], Harishchandra Singh [e,f], A.K. Yadav [g], Nainesh Patel [h], Pablo Ayala [c], Matjaž Spreitzer [a,b], Dominik Eder [c], Alexey Cherevan [c]

[a] Advanced Materials Department, Jožef Stefan Institute, Jamova 39, 1000 Ljubljana, Slovenia
[b] Jožef Stefan International Postgraduate School, Jamova 39, 1000 Ljubljana, Slovenia
[c] Institute of Materials Chemistry, TU Wien, 1060 Veinna, Austria
[d] Department of Physics, Faculty of Science, The M.S. University of Baroda, Vadodara 390002, India
[e] Nano and Molecular Systems Research Unit, University of Oulu, FIN-90014, Finland
[f] Amity Institute of Applied Sciences, Amity University Uttar Pradesh, Noida 201313, India
[g] Atomic & Molecular Physics Division, Bhabha Atomic Research Centre, Mumbai 400085, India
[h] Department of Physics and Electronics, Christ University, Bengaluru 560029, India

ARTICLE INFO

Keywords:
Graphitic carbon nitride
2D photocatalyst
Hydrogen evolution reaction
Dual-metal co-catalyst
Non-noble metals

ABSTRACT

Graphitic carbon nitride (g-C_3N_4) nanosheets are extensively used in photocatalytic applications but are often decorated with noble-metal co-catalysts to yield relevant efficiencies. Herein, we report a dual-metal co-catalyst system comprising cobalt and molybdenum (CoMo) nanoclusters uniformly integrated into heptazine g-C_3N_4 nanosheets for enhanced visible-light-driven hydrogen evolution reaction (HER). The intimate contact between metals as well as with gC_3N_4 layer was verified through X-ray absorption and X-ray photoelectron spectroscopies. Mechanistic insights obtained through a combination of experimental and computational studies suggest that Co acts as primary catalytic center, while Mo plays a preliminary role in facilitating surface hydrogen coverage, collectively accelerating the redox rates and achieving 10 times higher performance compared to bare gC_3N_4. Post-HER analysis reveals disintegration of co-catalyst into Co single-atoms, which then takes the leading role in sustaining the HER. The role of co-catalyst was mainly limited to the surface, acting as electron trap, reducing charge recombination and as a HER catalytic center. The composite exhibits excellent photostability over 13 h of ON/OFF illumination cycles, highlighting its potential for intermittent operations under practical conditions. This study presents a co-catalyst design strategy leveraging dual-metal synergy as a non-noble, scalable alternative to conventional noble-metal-based HER co-catalysts for solar fuel generation.

1. Introduction

Solar hydrogen (H_2) generation by photocatalytic water-splitting is one of the cleanest methods to harness the solar energy, reducing the stress on the deteriorating climate conditions [1,2]. It offers a promise to tap the perpetual sources of sun and water and convert them into usable forms of energy. H_2 also serves as a crucial raw material in multiple industries and solar H_2 production units can be locally setup to meet such industrial demands. However, photocatalytic water-splitting has remained an elusive challenge despite enormous research being conducted for over half a century [3,4]. In particular, for particle-based systems, the state-of-the-art solar to H_2 (STH) conversion efficiency has still remained below 1%, which is largely due to the lower catalytic rates of the photocatalysts being used [5,6]. The materials research has evolved over the decades and the current particulate photocatalyst systems usually comprises one (or more) photoabsorber(s) and a co-catalyst [7,8]. The photoabsorbers are typically semiconductors responsible for the photon-related steps in photocatalysis, namely light absorption, charge generation and transport to the surface. Each of these steps can be a rate-limiting process and hence the photo-absorbers are chosen and/or designed to ensure that they perform these tasks efficiently. Once the photo-generated charges reach the surface, they are

* Corresponding author at: Advanced Materials Department, Jožef Stefan Institute, Jamova 39, 1000 Ljubljana, Slovenia.
E-mail address: suraj.gupta@ijs.si (S. Gupta).

https://doi.org/10.1016/j.fuel.2026.140103
Received 30 January 2026; Received in revised form 25 May 2026; Accepted 27 May 2026
Available online 4 June 2026

transferred to the co-catalysts that function as the surface redox centers, performing the desired half-reactions. The final photocatalytic efficiencies are eventually determined by the synergistic performance of both these components (photoabsorbers and co-catalysts) and hence their development is of prime importance.

Two dimensional (2D) semiconductors are often preferred choices for photo-absorbers as their layered morphology not only improves light absorption but also offers lower diffusion length for photo-generated charges to reach the surface, thus preventing bulk recombination [9,10]. Amongst the known 2D semiconductors, the family of graphitic carbon nitride have been investigated extensively, owing to their tuneable bandgaps, morphologies, structure and robustness [11–13]. 3C:4N analogues of the family, typically formed by thermal condensation of the heptazine units, termed as gC_3N_4, are probably the most researched photocatalysts in the last two decades [14,15]. However, it is noteworthy that despite promising optical behaviour (bandgap ~2.7 eV) and favourable band edge positions for HER ($E_{CB} = -1.3$ V vs NHE) [16], gC_3N_4 becomes photo-active only with incorporation of noble-metal co-catalysts (Pt, Ru, Ag, etc.). The key reasons for the lower photo-response in pristine gC_3N_4 are associated with the photo-generated charge separation (high exciton binding energy) and transport (high recombination, low charge mobility) [14,17,18], which gets partially resolved by the use of noble-metal co-catalysts. To avoid their use, non-noble transition-metal-based co-catalysts have also been researched extensively but their performances are still not comparable to the noble metals [19,20].

Owing to their known HER properties, first-row transition metals (namely Co, Ni, Fe) are first choices when designing a new co-catalyst [21–23]. In our previous report, we integrated CoB nanoparticles into gC_3N_4 nanosheets, resulting in considerable improvement in photocatalytic HER rates, mediated by the higher redox activity of CoB nanoparticles [24]. Through computational modeling, it was observed that H atom has much higher affinity towards Co sites owing to its ideal electronic characteristics originating from the d-band electrons. Likewise, Co/gC_3N_4 [25], Co–P_i/gC_3N_4 [26], Ni/g-S-C_3N_4 [27], NiO/gC_3N_4 [28], FeP/gC_3N_4 [29], Ni_2P/gC_3N_4 [30] and similar composites are known to boost the HER rate due to the inclusion of transition-metals [21]. The performance of these non-noble co-catalysts can be further boosted through forming multi-metal co-catalysts, where the synergistic effect of the multiple metals can create a greater impact and improve the catalytic redox activity of the co-catalysts [31]. FeCo loaded gC_3N_4 showed an improved HER rate when compared to mono-metal co-catalysts (Fe-gC_3N_4, Co-gC_3N_4) [32]. Similar observations were made for other dual-metal co-catalyst systems combined with gC_3N_4, such as $Ni_xCo_{1-x}S$/gC_3N_4 [33], NiMo/gC_3N_4 [34], NiCu/gC_3N_4 [35], Mo-CoS_x/g-C_3N_4 [36], Co_3W_3C/g-C_3N_4 [37], etc.

To tap the advantage of dual-metal systems, in this work, we develop a dual-metal CoMo co-catalyst and integrate it with gC_3N_4 nanosheets to improve their photocatalytic HER performance. In electrochemical water-splitting, addition of a small amount of Mo (few at%) into Co catalyst is known to improve the HER rates considerably [38–40]. However, to the best of our knowledge, their application as a co-catalyst for gC_3N_4 has never been reported, imparting a unique novelty to this work. In this work, we introduce a novel CoMo dual-metal co-catalyst integrated with exfoliated g-C_3N_4 nanosheets. The formation and integration of the CoMo clusters were confirmed by electron microscopy and various spectroscopic tools. The improvement in photocatalytic HER was measured and quantified to establish the significantly higher performance of CoMo-gC_3N_4 catalyst, compared to bare gC_3N_4 as well as mono-metal-loaded co-catalyst. Based on the observed experimental results, a mechanistic pathway was proposed explaining the roles of Co and Mo in the composite catalyst. This work showcases a successful strategy to improve the photocatalytic HER rate of gC_3N_4 by using non-noble metal catalysts, while strengthening the case for the use of multi-metal co-catalysts in solar fuel production.

2. Experimental details

2.1. Synthesis of gC_3N_4 composites

Synthesis of gC_3N_4 nanosheets (NS) was performed by thermal condensation of melamine by heating it at 550 °C at a ramp rate of 5 °C/min and maintained for 4 h. The reaction was performed in a closed vessel to maintain the by-product (ammonia) pressure and equilibrate the condensation process. The procedure resulted in formation of bulk gC_3N_4 which was further exfoliated by ultrasonic treatment. To do so, 150 mg of bulk gC_3N_4 was dispersed in 250 mL of deionized water (DIW) and put under ultrasonic bath for 10 min. The suspension was dispersed further in an ice bath using an ultrasonic probe for 15 min with 2 s On – 1s Off cycle (2 kHz), resulting in highly dispersed gC_3N_4 nanosheets.

To incorporate the co-catalysts, gC_3N_4 nanosheet suspension was directly used. Appropriate amounts of $Na_2MoO_4.2H_20$ and $CoCl_2{\cdot}6H_2O$ were dissolved in 10 mL of DIW, successively, forming a mixture of Co and Mo ions (Co/Mo-precursor solution). The mixture was added to the gC_3N_4 nanosheet suspension in a dropwise manner, under continous stirring, to ensure that the metal ions are uniformly adsorbed on the surface of the nanosheets. In a separate beaker, $NaBH_4$ was dissolved in 10 mL DIW, with a boron to metal molar ratio of 3:1. After an hour of stirring the gC_3N_4/metal ion suspension, aqueous $NaBH_4$ solution was added to it in a dropwise manner, to reduce the metal ions, enabling their incorporation on the surface of the nanosheets. $NaBH_4$ is a strong reducing agent, causing exothermic reduction of metal ions in the solution to metal nanoparticles. Due to this exothermic process, the formed nanoparticles aggregate into bigger nanoclusters. To avoid this aggregation into larger nanoparticles, the temperature of the solution was maintained below 10 °C throughout the procedure. The mixture was stirred for another hour, before separating the suspension through centrifugation. The residue was washed several times with DIW and ethanol to remove the undissolved by-products and then dried in vacuum to obtain CoMo-gC_3N_4 composites. The ratio of Co and Mo in the Co/Mo precursor solution was varied in the mole ratio of 0.9:0.1, 0.8:0.2, 0.7:0.3, 0.6:0.4 and 0.5:0.5, while the nominal loading amount of co-catalyst was varied from 3, 5, 7, 11 to 13 wt%. Co-gC_3N_4 and Mo-gC_3N_4 composites were also prepared using the same procedure, with only Co and Mo precursors, respectively with 9 wt% loading.

2.2. Materials characterization

Structural information was obtained through X-ray diffraction (XRD) patterns recorded in a θ-2θ configuration using a Bruker AXS D4 Endeavor with Cu Kα radiation (λ = 1.5414 Å). The morphological characteristics were analyzed through scanning electron microscopy (SEM) using a Verios HP 4G (Thermo Fiscer) operating at 2 kV. Transmission electron microscopy (TEM) was carried out with a JEOL JEM-2100 instrument, while scanning transmission electron microscopy (STEM) was performed using Cs-corrected microscope Spectra 300 (Thermo Fisher, Netherlands) operated at 200 kV, equipped with four 30 mm^2 windowless collimated SDD spectrometers for sensitive detection of elements present in low amounts. Surface chemical states were examined via X-ray photoelectron spectroscopy (XPS) on a PHI Versa Probe III, utilizing Al Kα radiation at 1486.6 eV. The C1s peak at 284.8 eV served as a reference, and the acquired XPS spectra were analyzed using Multipak software (PHI). Absorption spectra was recorded in diffuse reflectance mode with an Agilent Cary 300 UV–vis spectrophotometer. Diffuse reflectance infrared Fourier transform spectroscopy (DRIFTS) was recorded with the powder samples diluted in KBr, which also acted as the background, using a Perkin Elmer Spectrum 400 FT-IR spectrometer. Bandgap was determined through Tauc plots, considering an exponent of ½, based on the reported indirect bandgap of gC_3N_4 [41,42]. Specific surface area of the samples were determined using Brunauer-Emmett-Teller (BET) method on a Micromeritic system with liquid nitrogen. Photoluminescence (PL) measurements were performed

using a PicoQuant FluoTime 300 spectrophotometer. A Xe arc lamp (300 W power) was used as the excitation source which was coupled with a double-grating monochromator. The detection system was composed of a PMA Hybrid 07 detector along with a high-resolution double monochromator. For steady-state measurements, 370 nm excitation wavelength was selected with 395 nm cut off filter to examine gC_3N_4 when different amounts of co-catalysts are loaded. The data was fitted using EasyTau2 software using 3 exponential functions.

Quantitative elemental analysis of the co-catalyst loading on the support was performed by X-ray fluorescence spectroscopy in total reflection geometry (TXRF) using an ATOMIKA 8030C spectrometer (Atomika Instruments GmbH, Oberschleissheim, Munich, Germany). The selected excitation source was the continuous spectrum of tungsten monochromatized at 35 keV (X-ray tube at 50 kV and 47 mA), samples were irradiated for 100 s and the characteristic X-rays were acquired with a Si(Li)-detector. Aqueous suspensions (c = 1 mg/mL) of the CoMo-g-C_3N_4 samples were prepared and an yttrium (Y) internal standard was added for quantification (final c = 0.01 mg/mL). The suspensions were sonicated for 30 min and vortexed for 5 min before drop casting a 5 μL aliquot on the quartz reflector, which was then dried on a hot plate. The residue was sealed with further 5 μL of a 1% PVA solution and then measured. Absolute amounts of Co and Mo were quantified with respect to the known Y amount, enabling the determination of the loadings on the g-C_3N_4 support.

The X-ray absorption spectroscopy (XAS) measurements were carried out at the SIRIUS beamline, SOLEIL synchrotron, France [43]. Local structure around the absorbing atom was obtained through quantitative analysis of Extended X-ray Absorption Fine Structure (EXAFS) spectra using the Demeter software package [44]. The software package was also used for EXAFS data analysis, which includes background reduction, Fourier transform to derive the versus R plots from the absorption spectra (using ATHENA software), generation of the theoretical EXAFS spectra starting from an assumed crystallographic structure, and finally fitting of experimental data with the theoretical spectra using ARTEMIS software [45].

2.3. Photocatalytic setup

Photocatalytic hydrogen evolution reaction (HER) experiments were conducted using a custom-designed glass slurry reactors with side illumination using a monochromatic 445 nm centered LED light source (SOLIS, Thorlabs). To maintain a stable temperature, the reactor solution was cooled to 15 °C using a water-cooling system (Lauda), and continuous stirring at 300 rpm ensured uniform suspension. In a typical experiment, the photocatalyst powder (0.5 mg/mL) was dispersed in the corresponding amount of 0.1 M triethanolamine (TEOA) solution via sonication for 3 min. This suspension was then transferred to the reactor, which was operated in either batch or flow mode, each utilizing distinct detection systems. For batch-mode experiments, the sealed reactor (total solution volume of 2 mL) was purged with argon gas at a flow rate of 10 mL min^{-1} (regulated by a mass flow controller from MCC-Instruments) for 10 min to eliminate dissolved oxygen and CO_2. To verify the successful removal of these gases, a 200 μL gas sample was extracted from the reactor headspace using a gas-tight Hamilton syringe and analyzed via gas chromatography (GC-2030, Shimadzu) with a Micropacked-ST column (ShinCarbon) and a barrier discharge ionization detector (BID). The chromatogram confirmed the absence of H_2 before illumination. Once the light source was activated, photocatalytically generated hydrogen was accumulated in the reactor headspace. Gas samples (200 μL) were taken at specific time intervals and analyzed using GC. The resulting H_2 concentrations (ppm) were converted into μmol values using the ideal gas law, considering the reactor's headspace volume. In flow-mode experiments, another reactor was used (total solution volume of 10 mL), which was flushed with Ar carrier gas continuously at a flow rate of 15 mL min^{-1}, ensuring the immediate transfer of reaction products to an online gas analyzer (Xstream, Emerson Process Management) equipped with a thermal conductivity detector [46]. After the baseline stabilized, indicating no hydrogen in the flow, the light source was switched on, and H_2 evolution was directly monitored in the gas stream. Measured H_2 concentrations (ppm) were converted into HER rates (μmol h^{-1}) using the ideal gas law, accounting for the continuous gas flow (15 mL min^{-1}).

2.4. Photo-electrochemical measurements

For photo-electrochemical measurements, the powder catalysts were deposited on a 5 mm glassy carbon electrode (L-shaped). For the deposition, a catalyst ink was prepared by dispersing 3 mg powder in 1 mL of solvent (0.75 mL DIW + 0.25 mL isopropyl alcohol + 10 μL Nafion) using ultrasonic treatment. This catalyst ink was drop-casted on the glassy carbon surface (0.3 mg·cm^{-2}), which then served as a working electrode, along with a graphite rod (counter) and a reversible hydrogen electrode (Mini-HydroFlex, Gaskatel). A quartz cubic reactor was used with ~100 mL of electrolyte (1 M KOH, N_2 purged). The catalyst surface was illuminated by a 300 W Xe lamp (Newport), fitted with an AM1.5G filter. The lamp intensity was calibrated to 1 sun illumination (100 mW·cm^{-2}) using a Si reference cell (Newport). All the electrochemical measurements were performed under light illumination, using a Gamry potentiostat (1010E). Linear sweep voltammetry was carried out at a scan rate of 10 mVs^{-1}. Electrochemical impedance spectroscopy (EIS) was performed at an applied potential of −0.5 V (vs OCP) within the frequency range of 200 kHz to 0.1 Hz, with a sine wave of 5 mV amplitude. Mott-Schottky measurements were performed at a frequency of 1 kHz.

2.5. Computational details

Density Functional Theory (DFT), as implemented in the QUANTUM ESPRESSO code [47] was employed to compute the structural, electronic and catalytic properties of the Co cluster on g-C_3N_4 (referred to as Co-gCN) and Mo-incorporated Co-g-C_3N_4 (referred to as CoMo-gCN). A Co_{13} cluster with icosahedral (I_h) symmetry is reported to be one of the most stable structures, compared to lesser number of Co atoms, and was thus considered here to match the experimental small sized co-catalyst nanoparticles [48–50]. Our initial investigation involved placing the Co_{13} cluster over 2 × 2 × 1 supercell of g-CN. As structure of the g-CN includes voids and web-like regions [51], structural optimization was performed to determine the energetically favoured adsorption site for the Co_{13} cluster. Subsequently, molybdenum was introduced into the Co-gCN structure by replacing two Co atoms, resulting in a Mo concentration of 15.3% (yielding Co:Mo ratio of 5.53), matching well with

Table 1
CoMo weight percentage on gCN determined through X-ray fluorescence in total reflection geometry (TXRF) for the samples with a nominal Co:Mo molar ratio of 0.7:0.3 (Co/Mo = 2.3).

Sample name	Loading (wt%) – with respect to CoMo-gCN			
	Co	Mo	Total wt%	Actual Co: Mo molar ratio
3CoMo-gCN	0.64 ± 0.06	0.12 ± 0.01	0.76 ± 0.08	8.7
5CoMo-gCN	2.25 ± 0.22	0.67 ± 0.07	2.92 ± 0.29	5.5
7CoMo-gCN	2.78 ± 0.28	0.57 ± 0.06	3.35 ± 0.34	7.9
11CoMo-gCN	3.86 ± 0.39	0.96 ± 0.10	4.82 ± 0.48	6.5
13CoMo-gCN	5.95 ± 0.60	0.73 ± 0.07	6.68 ± 0.67	13.2
5Co-gCN	0.19	–		–
5Mo-gCN	–	Not detected		–

the experimentally observed Co:Mo ratio of 5.5 (see Table 1, 5CoMo-gCN). The final structure maintained the symmetry of the Co cluster during the structural optimization over gCN. This optimized CoMo-gCN structure was then utilized to determine the HER activity over the Co and Mo atoms and their respective bonding regions.

For the calculations, we utilized a plane wave basis set and ultrasoft pseudopotentials. The Perdew-Burke-Ernzerhof (PBE) exchange–correlation functional, a component of the Generalized Gradient Approximation (GGA) [52], was chosen as exchange–correlation functional. To accurately describe the valence electron wave function, we used a plane wave basis set with a 60 Ry wave function cutoff and a 600 Ry charge density cutoff. For structural relaxation, a Γ-centered 4 × 4 × 1 k-mesh grid was used, while an 8 × 8 × 1 k-mesh grid was employed for electronic property calculations. To prevent spurious electronic interactions with periodic images during all the calculations, a 10 Å of additional vacuum layer was applied in a perpendicular direction of the system. Grimme-d2 [53] correction was applied to account for the Van der Waals interactions.

Both models were investigated for the HER using the Computational Hydrogen Electrode (CHE) method, as described by Nørskov and his group [54]. The CHE method involves calculating the adsorption energy of the reaction intermediate on the catalyst's surface using the thermodynamic approach ignoring any reaction barriers separating the reaction intermediates. Further, Gibbs free energy for each intermediate step was evaluated to identify the rate determining step of the reaction. This step is identified by the reaction's highest energy barrier, also known as the overpotential (more details in supporting information).

3. Results and discussion

3.1. Materials investigations

Formation of bulk gC_3N_4 is a relatively straightforward process that involves the thermal condensation of nitrogen-rich precursors such as melamine, urea, thiourea, or dicyandiamide [19]. These precursors polymerize upon heating (~400–600 °C) in a controlled atmosphere (often air or nitrogen), leading to the formation of layered gC_3N_4 structures. However, their exfoliation into thinner sheets is typically accomplished by chemical, thermal and ultrasonic methods. Chemical exfoliation often involves treatment with strong acids (H_2SO_4, HCl) or their mixtures, which may introduce surface functional groups or heteroatom doping (e.g. with oxygen, sulfur), thereby altering the chemical, optical and electronic properties of gC_3N_4 [55,56]. Similarly, thermal treatment may lead to partial decomposition or crystallization of the polymeric units, which again affects the gC_3N_4 properties [57,58]. It must be noted that some of these alterations benefit the photocatalytic activity of gC_3N_4, though they might be unintentional. A simpler, non-destructive strategy for exfoliation is through ultrasonic treatment, which does not involve the risk of chemical or structural alterations. To intensify and accelerate the exfoliation process, an ultrasonic probe was used, which resulted in homogeneously dispersed gC_3N_4 nanosheets, suspended in water. This suspension also serves as a suitable medium to dissolve the metal ion precursors for co-catalyst integration.

Incorporation of single metal co-catalysts in gC_3N_4 NS have been frequently reported, but using dual metal co-catalysts poses different challenges with respect to their optimization. One of the key factors is the ratio of the two metals that eventually defines the redox behaviour while the other is the co-catalyst loading, which affects the surface coverage of gC_3N_4 and may impact the solar light absorption. To optimize the ratio between Co and Mo, a catalyst loading of 9 wt% was fixed (based on a previous optimization [24]) while the nominal molar ratio of Co:Mo were varied as 0.9:0.1, 0.8:0.2, 0.7:0.3, 0.6:0.4 and 0.5:0.5. Powder XRD (Fig. S1a) showed similar patterns for all the compositions, with a (002) reflection at 27.2°, characteristic of the interlayer stacking of heptazine sheets in gC_3N_4 [59]. Based on the measured hydrogen generation rates (HGRs) (Fig. S1b), it was observed that the performance increases with increasing nominal Mo concentration and reaches a maximum for the nominal Co:Mo ratio of 0.7:0.3, following which the HGR starts declining. This result showcases that addition of Mo (in small amount) significantly improves the HGR while Co atoms might provide the main active centers as the HGR decreases with decreasing Co concentration. Nevertheless, too high Co content is also not beneficial, which underlines the synergic effect of the co-integration of both Co and Mo atoms in specific ratios. Further, with a fixed initial nominal Co:Mo ratio of 0.7:0.3, the co-catalyst loading was varied to optimize the surface coverage over the gC_3N_4 NS. The composites with different loading of cobalt and molybdenium are represented (denoted) as xCoMo-gCN, where x = 3, 5, 7, 11 or 13 wt% and correspond to the nominal weight of the co-catalyst with respect to gC_3N_4, while the initial nominal Co:Mo molar ratio was 0.7:0.3. Likewise, Co and Mo loaded (nominal 5 wt%) single-metal co-catalyst composites are represented as Co-gCN and Mo-gCN, respectively, whereas bare gC_3N_4 is termed as gCN. Based on their HGR profiles (Fig. S2), the catalyst loading with nominal 5 wt% (5CoMo-gCN) proves to be the optimum amount and the activity declines at higher loading, which might be an effect of the excess coverage of the gCN surface preventing light absorption. It is noteworthy that the actual catalyst loading is different from the expected amount as detected from TXRF data (Table 1). For instance, 5CoMo-gCN shows a total co-catalyst loading of 2.92 wt%, which is lower than the anticipated 5 wt %. Notably, the loading of cobalt on gCN is much more efficient compared to molybdenum, resulting in larger final Co:Mo molar ratio, varying between 5.5 and 13.2 (Table 1). This clearly indicates that not all the precursor metal ions are deposited on the gCN surface and some of them might be washed out during the synthesis procedure. However, the total co-catalyst content increases steadily with the increasing precursor amount and represent an ideal situation to compare different loading ratios (Table 1). For simplicity, we will continue using the same catalyst notations (xCoMo-gCN) for different mass loadings, where "x" in xCoMo-gCN refers to the nominal weight percentage, and the actual values are provided in Table 1.

The XRD patterns for xCoMo-gCN composites (Fig. 1a) show a reduced intensity of the reflections at 27.2°. This reduction in intensity is directly related to the delamination of the stacked gCN layers, which might be a consequence of the co-catalyst integration. Moreover, a tiny feature at 12.6°, representing (100) reflections originating from the heptazine repeating units is also observed in bare gCN [59,60]. This feature vanishes after co-catalyst loading, indicating disruption of the in-plane structural order and fragmentation of the heptazine units. Notably, 5Mo-gCN (Fig. 1b) portrays XRD features similar to bare gCN, with visible reflections at both 12.6° and 27.2°, indicating no structural alteration after the treatment of gCN in water suspension together with dissolved Na_2MoO_4 and in the presence of $NaBH_4$. Furthermore, TXRF analysis showed no molybdenum detected in the 5Mo-gCN sample (Table 1). This was further verified through STEM images of 5Mo-gCN (Fig. S3a-b), which shows the renowned planar sheet-like structures of gC_3N_4, without any nanoparticle formation on their surface. EDS maps and spectra (Fig. S3c) indicate the presence of C, N and O only, with no signatures of Mo, confirming the TXRF data. To explain the absence of Mo, we consider the dissolution mechanism of Na_2MoO_4 in water, forming MoO_4^{2-} ions ($Na_2MoO_4 \rightarrow 2Na^+_{(aq)} + MoO^{2-}_{4(aq)}$). gCN nanosheets possess negative zeta potential[24], which leads to a repulsive force with negatively charged MoO_4^{2-}, eventually preventing its deposition. Alternately, the XRD reflections of 5Co-gCN and 5CoMo-gCN do not show the 12.6° signature, confirming that Co inclusion primarily leads to in-plane and inter-plane modifications of gCN. Adhesion of Co^{2+} ions on the gCN NS is favourable due to the negative zeta potential of gCN, inducing an attractive force towards Co^{2+}. As it is evident from Table 1, in the presence of Co^{2+} ions, molybdenum species are also adsorbed on the gCN, suggesting that Co^{2+} plays an important role on the molybdenum uptake. Notably, in all cases, Mo adsorbed less efficiently than Co and the best molybdenum uptake was observed for the 5CoMo-gCN sample (Table 1), which showed the best HGR. Considering the

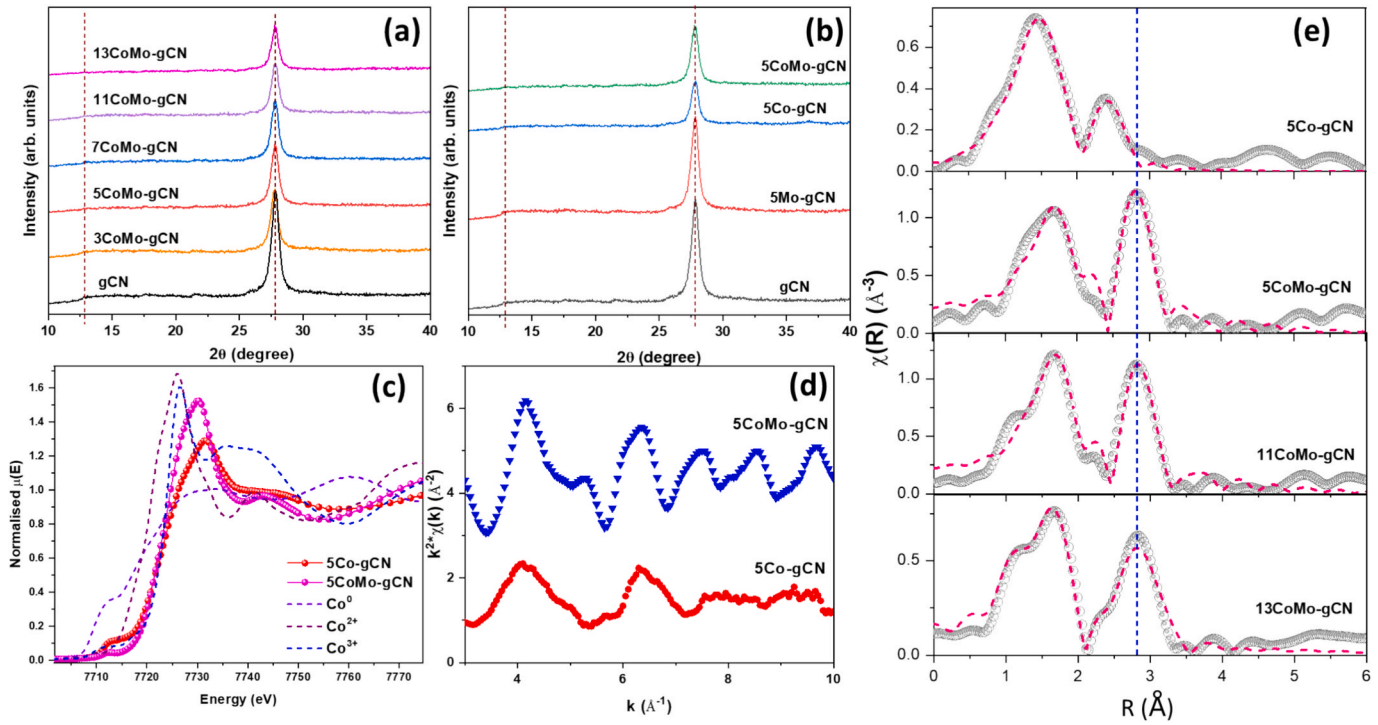

Fig. 1. XRD patterns for (a) bare gCN and CoMo-gCN with different mass loadings; (b) bare gCN compared to 5Co-gCN, 5Mo-gCN and 5CoMo-gCN; (c) Normalized XANES spectra at Co K-edge of 5Co-gCN and 5CoMo-gCN along with Cobalt references; (d) EXAFS oscillation obtained after background subtraction of 5Co-gCN and 5CoMo-gCN; (e) Fourier transform EXAFS spectra (scatter points) of 5Co-gCN along with increasing mass loading of CoMo-gCN and their respective fits (dashed lines). The k = 3–10 $Å^{-1}$ range is used for Fourier transform and fitting range is used from 1 to 3.5 Å.

bonding (interaction) between cobalt and molybdenum, as observed from EXAFS spectra (discussed later), it is most plausible that molybdenum ions adsorb on the g-CN sites that are already covered by cobalt cations (Scheme 1). This can be best illustrated by the attractive forces between Co^{2+} and MoO_4^{2-} ions. In our system $NaBH_4$ acted as reducing agent to form CoMo-gCN composite. According to the standard reduction potentials of Co^{2+} ($Co^{2+} + 2e^- \rightarrow Co^{\circ}_{(s)}$, $E^{\circ} = -0.282$ V) and MoO_4^{2-} ($MoO_4^{2-} + 4H_2O + 6e^- \rightarrow Mo^{\circ}_{(s)} + 8OH^-$, $E^{\circ} = -0.926$ V), the reduction of Co^{2+} into metallic Co° is far more facile under the reported experimental conditions compared to the reduction of MoO_4^{2-} into metallic Mo. These facts are well supported by the literature reports. Specifically, Chen et al. [61] deposited metallic Co° nanoparticles on $ZnIn_2S_2$ by different methods, including reduction of Co^{2+} into Co° by $NaBH_4$ as well as by in-situ photoreduction. Similarly, Thabet et al. [62] reported in-situ photocatalytic deposition of Co° nanoparticles on TiO_2 through photon energy-assisted methanol reduction of Co^{2+} ions. On the contrary, Tsang et al. [63] observed that the reduction of Na_2MoO_4 with $NaBH_4$ in water solutions resulted in molybdenum oxide with lower oxidation states (e.g. MoO_2). Although the reduction of Co^{2+} into Co° is facile, the oxidation back to Co^{2+} also occurs easily in air [61].

To establish an understanding of the local structure of the CoMo co-catalyst, XAS studies were performed. The normalized XANES spectra at the Co K-edge (Fig. 1c) was recorded for 5Co-gCN and 5CoMo-gCN, alongside the standard Co metal, as well as Co^{2+} and Co^{3+} references. When compared to metallic Co, the contributions from 5Co-gCN and 5CoMo-gCN are shifted to higher energy, with a relatively intense pre-edge hump around 7713 eV. The absorption edge coincides with that of $LaCoO_3$, indicating the presence of bulk Co in the +3 oxidation state while the shift suggests ionic bonding. A sharp white line at 7730 eV further suggests Co-N/C type ionic bonding, originating from the interaction between Co atoms and gCN underlayer [64]. The EXAFS oscillations (Fig. 1d) and the Fourier transformed (FT) EXAFS spectra (Fig. 1e) were used to obtain the local structure around the absorbing Co atoms. The FT spectrum of 5Co-gCN shows a strong coordination peak around 1.45 Å and 2.01 Å which is usually due to surrounding Co-N/C type scatterers. Furthermore, an intense second peak around 2.40 Å for 5Co-gCN is attributed to Co-Co scatterers from next near neighboring atoms. A similar set of coordination peaks are observed in 5CoMo-gCN. However, a distinct second coordination peak around 2.80 Å (marked with vertical dashed line in Fig. 1e) is further observed in 5CoMo-gCN arising due to the contribution from Co-Mo scatterers. The result was verified with 11CoMo-gCN and 13CoMo-gCN samples, all indicating the

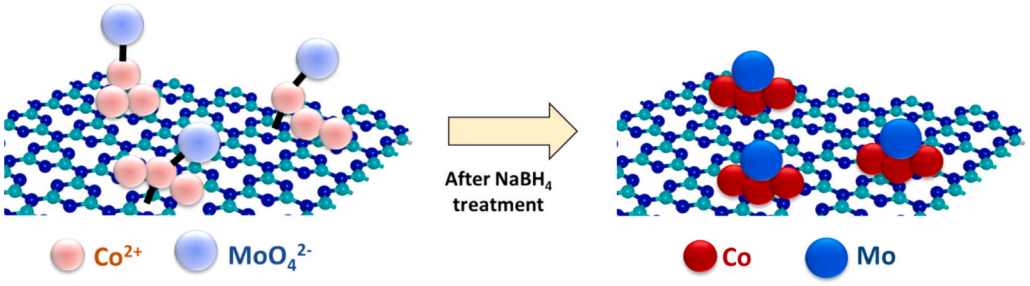

Scheme 1. Representation of the Co^{2+} mediated adsorption of MoO_4^{2-} anions on gCN and subsequent formation of CoMo-gCN composite.

coordination of Mo atoms in the Co neighboring shells, confirming the formation of Co-Mo bonds in the co-catalyst. Based on the fitting results (Table S1), the average Co-N/C and Co-Co bond lengths appear to have increased in 5CoMo-gCN (2.14 Å and 3.12 Å, respectively) when compared to 5Co-gCN (1.99 Å and 2.58 Å, respectively). This expansion can be attributed to the incorporation of Mo atoms in the local coordination environment of Co. Given that Mo (145 pm) possesses a slightly larger atomic radius than Co (135 pm), its presence in neighboring atomic shells induces a lattice distortion, leading to elongated bond distances. Notably, the coordination number for Co–Co decreases significantly in 5CoMo-gCN (1.99) compared to 5Co-gCN (3.80), accompanied by a marked increase in Co–Mo coordination (3.88). This change in local atomic environment provides further evidence for the successful formation of a Co–Mo bimetallic catalyst structure and supports our hypothesis on Co^{2+} being the link joining MoO_4^{2-} and gCN. A similar XAS experiment was tried at the Mo L-edge (2.52 keV), but it falls at the very limit of the lower energy range of the synchrotron's monochromator (2.5–13 keV), making it exceedingly difficult to acquire data of sufficient quality. It was further complicated by the lower content of Mo, compared to Co (0.67 wt% of Mo in 5CoMo-gCN from TXRF), due to which no reliable signals were obtained from the sample.

XAS analysis confirms the local co-ordination of Co and Mo atoms in the CoMo co-catalyst and hints at the possible interaction between Co and gCN layer. The data was complemented by XPS analysis, with a detailed information about the surface chemical states and the elemental composition of the composites, including that of Mo, which could not be confirmed with XAS reliably. C 1s spectrum (Fig. 2a) showed typical features of C–C, N–C–N and O–C–O species, with marginally higher binding energies (BEs) for the co-catalyst loaded samples. A similar behaviour with more pronounced BE shift was observed in N 1s states (Fig. 2b) for all the three peaks corresponding to N–C–N, N-$(C)_3$ and C–NH_2 in both the composite samples [65]. This behaviour is an indication of the electronic transfer from the gCN layers to the co-catalyst clusters, indicative of the interaction predicted from XAS. The BE shift in N1s is not observed in 5Mo-gCN, as no co-catalyst integration was found here. In 5Co-gCN (Fig. 2c), Co 2p spectra shows peaks at 780.5 and 782.5 eV with corresponding satellites that are assigned to Co^{3+} and Co^{2+} states, respectively [66]. The presence of Co^{3+} state was also observed from XAS while Co^{2+} may arise due to the surface adsorption of hydroxyl groups ($Co(OH)_2$) from the ambient atmosphere, which is often observed in metallic Co surfaces. 5CoMo-gCN (Fig. 2a) shows a similar set of peaks with the exception that all the peaks are marginally shifted, which may be due to the electronic interaction with adjacent Mo atoms. From Mo 3d spectra (Fig. 2d) in 5CoMo-gCN, Mo is found to exist in Mo^{6+} state, suggesting surface oxidation similar to Co. Notably, there is no visible peak for 5Mo-gCN in Mo 3d state, reinstating the absence of Mo in the sample (inset of Fig. 2d). O 1s spectra (Fig. 2e) of bare gCN shows two tiny BE peaks at 532.0 and 533.7 eV, which could be due to the surface adsorbed carbonates. In 5Co-gCN and 5CoMo-gCN, O 1s species appear different from bare gCN, with a main peak at 531.3 eV, which again corresponds to surface $Co(OH)_2$, reminiscent of the adsorbed hydroxyl groups [66]. These surface hydroxyl groups are also observed from the DRIFTS spectra (Fig. 2f) which shows a clear hump at 3536 cm^{-1} in co-catalyst loaded samples (except 5Mo-gCN), where the hump intensity increases with higher co-catalyst loading. This hump arises due to hydroxylation of the metallic (Co or Mo) surface while bare gCN shows lower affinity towards the adsorption of hydroxyl groups on the surface, matching well with the O 1 s spectra for bare gCN. The full DRIFTS spectra show typical features of gCN network with signatures of NH stretching (~3060–3300 cm^{-1}), CN heterocycles (1100–1700 cm^{-1}) and peaks representing heptazine units (810 cm^{-1} and 891 cm^{-1}) [67,68]. Notably, none of these features show a variation due to co-catalyst integration.

The structural and chemical analysis confirms the successful integration of CoMo co-catalysts on gCN surface, with electronic interchange between them. More details about the morphology were

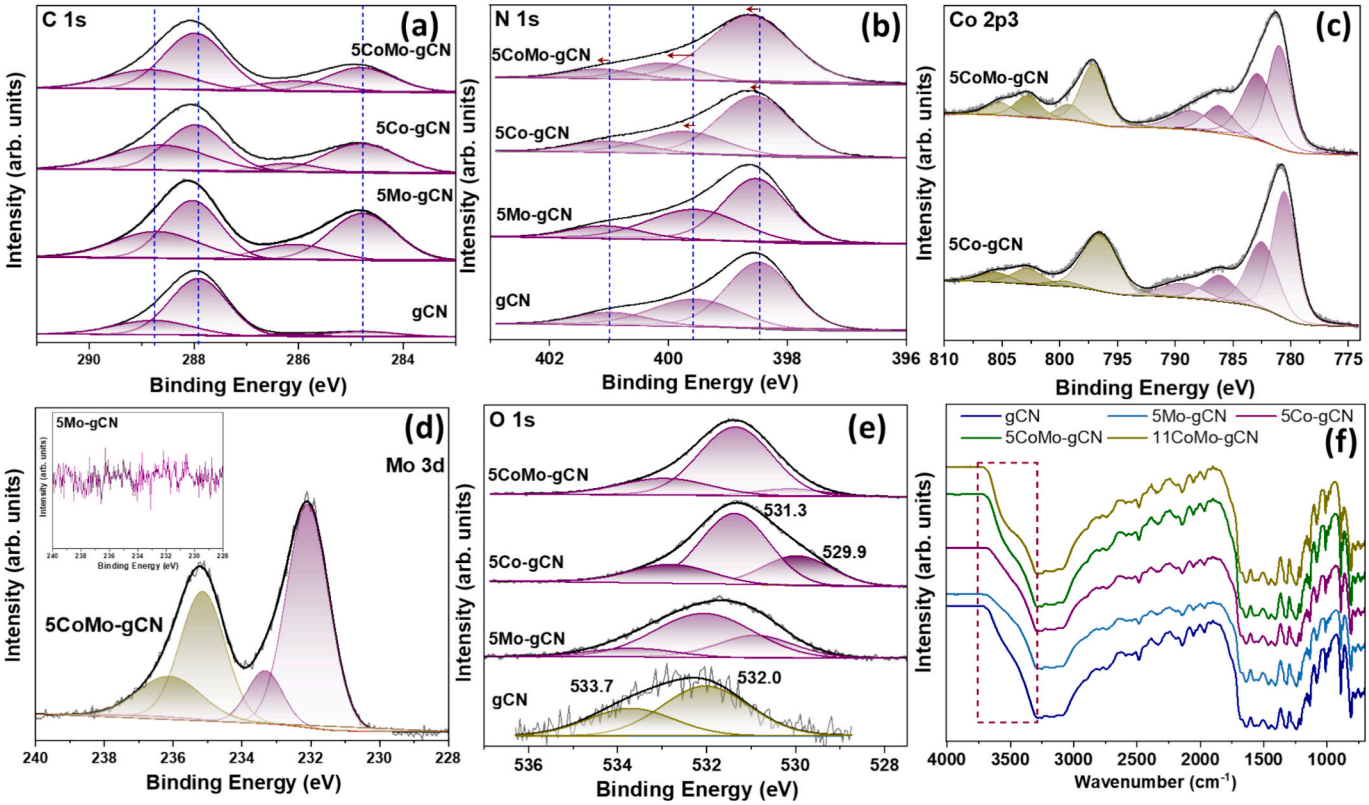

Fig. 2. High-resolution XPS spectra for (a) C 1s, (b) N 1s and (e) O 1s in bare gCN, 5Co-gCN, 5Mo-gCN and 5CoMo-gCN; (c) Co 2p in 5Co-gCN, 5CoMo-gCN and (d) Mo 3d in 5Mo-gCN (inset) and 5CoMo-gCN; (f) DRIFTS spectra for bare gCN, 5Co-gCN, 5Mo-gCN and representative CoMo-gCN composites.

obtained through electron microscopy. SEM images show the sheet-like morphology of gCN in all samples without any larger aggregation of co-catalyst particles (Fig. S4). As there was no morphological variation, the BET surface areas obtained for all the samples were also similar in the range of 21–23 m^2g^{-1} (Table S2). The nitrogen adsorption–desorption isotherms (Fig. S5) exhibit a Type II profile (IUPAC) [69], indicating the presence of non-porous or macroporous structures. A slight hysteresis loop, resembling a Type H3 behavior, is also observed, suggesting the presence of aggregated plate-like particles with slit-shaped mesopores. From TEM investigations, the integration of small metallic nanoclusters with average size of ~4–5 nm becomes evident as the nanoclusters are uniformly dispersed over the gCN layers (Fig. 3a and b). The ultra-small size of the co-catalyst clusters explains the absence of their reflections in the XRD profile. Elemental mapping and spectrum from TEM-EDS (Fig. 3c and d) portrays that the nanoclusters are composed of both Co and Mo with homogeneous distribution over background gCN sheet containing carbon and nitrogen.

Information about the light absorption properties of the gCN composites were obtained through diffused reflectance spectroscopy (DRS). All the co-catalyst loaded gCN composites showed similar light absorption as that of bare gCN, absorbing wavelengths in the visible region (<450 nm) (Fig. 4a). xCoMo-gCN samples show absorption in the similar range of wavelengths, suggesting no observable change in the optical behaviour due to increasing loading (Fig. 4b). The optical bandgap of bare gCN as well as co-catalyst composites were almost identical, matching the reported value of 2.75 – 2.8 eV for gCN (Fig. S6) [70]. This indicates that the co-catalyst integration did not significantly alter the electronic band structure of gCN. The unchanged bandgap suggests that the dual-metal species were primarily incorporated on the surface of gCN nanosheets and the interaction is limited to the surface, rather than modifying the intrinsic electronic states of gCN or introducing deep defect levels.

3.2. HER investigations

The photocatalytic performance of the optimized composites was evaluated for HER in a pure water solution (pH 7). To avoid the possibility of back reactions (oxidation of hydrogen) due to the photogenerated holes, 10% TEOA was added as the hole scavenger [71]. The HER rate for the dual metal co-catalyst integrated gCN composite (5CoMo-gCN) was higher by an order of magnitude when compared to bare gCN (Fig. 5a). Even when compared to 5Co-gCN, containing a single-metal co-catalyst, the HER rate for 5CoMo-gCN was almost two times higher, highlighting the promoting effect of the co-existence of Co and Mo in the dual metal co-catalyst system. Similar enhancement in HER activity in CoMo-based catalysts have been observed for electrocatalytic water-splitting [39,40]. 5 wt% Pt decorated gCN (5Pt-gCN) was used as a benchmark and it remains the best catalyst, but the performance of 5CoMo-gCN is still noticeably high considering a completely non-noble catalyst. A summary of other non-noble co-catalyst/gC_3N_4 composites used for photocatalytic HER is shown in Table S3. In catalysts containing Mo, it has been proposed that Mo (oxide) centers can

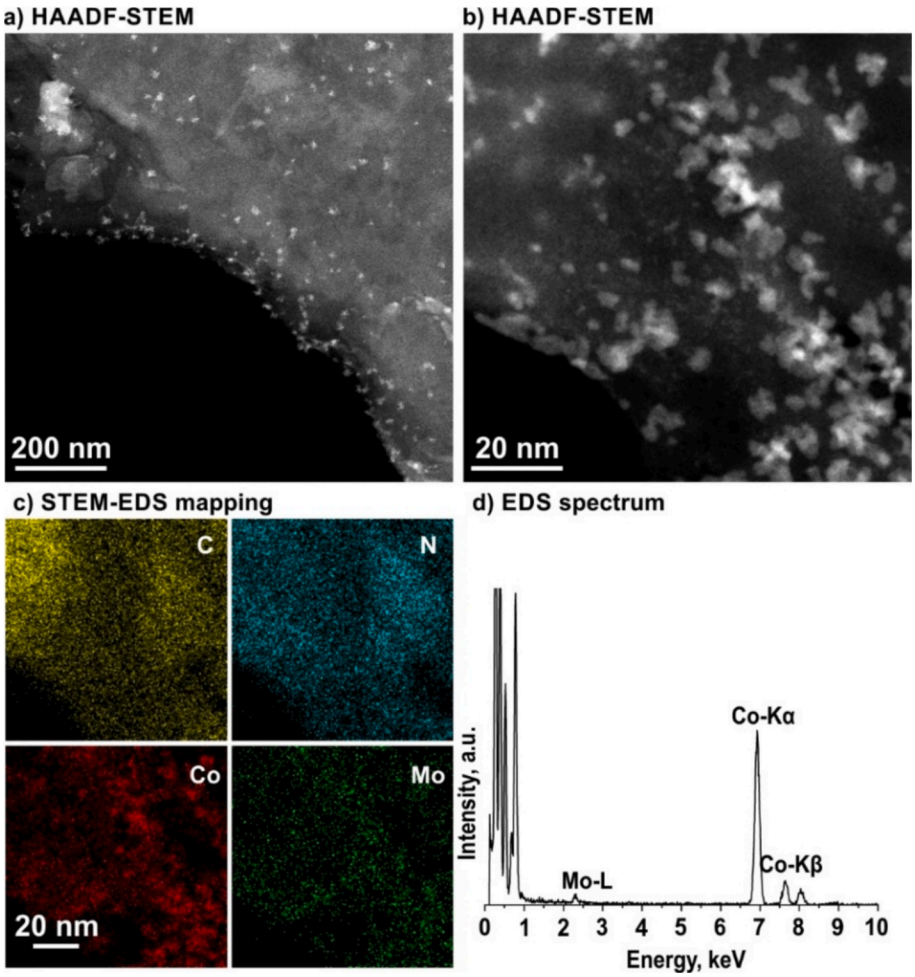

Fig. 3. (a) Low-magnification HAADF-STEM image showing uniform distribution of the CoMo nanoparticles with brighter contrast on the gCN sheet in 5CoMo-gCN. (b) Image at higher magnification discloses the ultrafine size of the CoMo co-catalyst particles in the range of 5 nm (c) STEM-EDS maps of the area in (b) confirming the presence of C and N in the substrate sheets, whereas Co and Mo signals stem from the NPs. (d) Average EDS spectrum of the area.

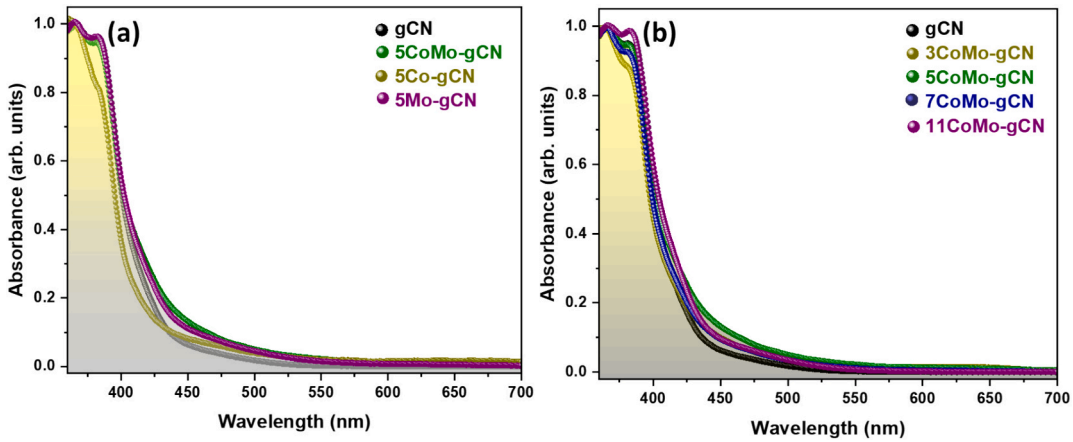

Fig. 4. Optical absorbance spectra determined through diffused reflecatnce spectroscopy for (a) bare gCN, 5Co-gCN, 5Mo-gCN and 5CoMo-gCN and (b) representative CoMo-gCN composites. The shaded part repesents the absobed portion of the solar radiation.

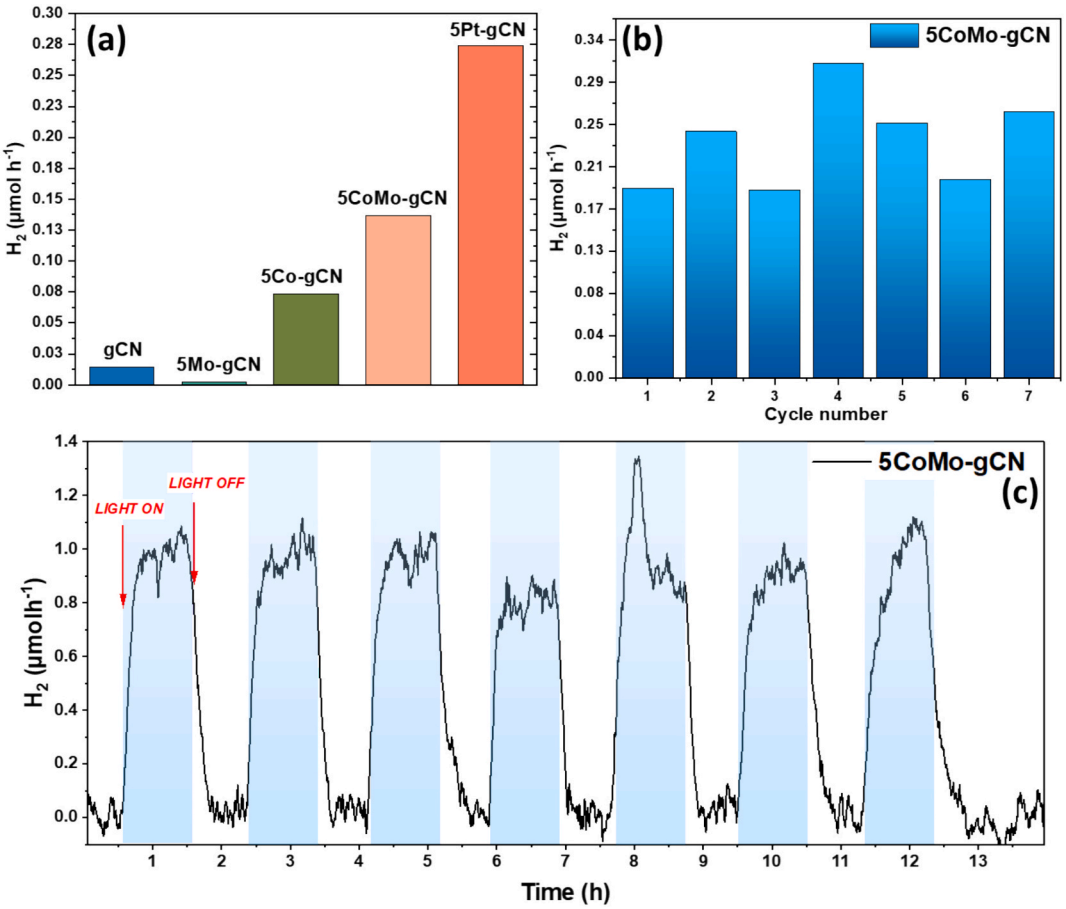

Fig. 5. (a) Comparison of the hydrogen generation rate for bare gCN, 5Co-gCN, 5Mo-gCN, 5Pt-gCN and 5CoMo-gCN using batch HER setup; (b) Hydrogen generation rate for 5CoMo-gCN during 7 cycles of photocatalytic testing using batch HER setup; (c) Stability test for 5CoMo-gCN portraying the behaviour under ON/OFF illumination cycles conducted for 13 h using flow HER setup.

form and stabilize surface hydrides during HER [72,73], which we believe makes it easier for Co-sites to facilitate HER. Notably, Co and Mo lie on the opposite sides of the semi-empirical Volcano plot, representing the metal-hydrogen bonding energies with intrinsic current densities [74]. Their co-existence and electronic interaction in CoMo co-catalyst may further modulate the electronic structure of Co, driving the H-bonding energy close to the desired peak of the volcano, eventually optimizing H adsorption and desorption mechanism. Thus, the synergy between the Co and Mo sites is responsible for the improved redox rates in 5CoMo-gCN. For any photocatalyst, it is extremely crucial to maintain its catalytic activity without any losses under intermittent solar irradiation. To mimic such conditions for 5CoMo-gCN, the HER rate was measured multiple times in successive light on–off cycles (Fig. 5b) in a batch reactor. It was observed that the average rate for each cycle was well-maintained (0.23 ± 0.04 μmol h^{-1}), confirming that the catalyst does not undergo deactivation or degradation during such dynamic

operation conditions. The dynamic photo-response behaviour with long-term stability was further validated in a flow reactor through instantaneous rise/decay of HER rate with light switching (Fig. 5c). The behaviour was consistently stable even after 13 h of measurement, testifying the stability of the composite catalyst.

To gain deeper insights into the photo-redox properties of the synthesized photocatalysts, photoelectrochemical tests were performed by depositing the materials on glassy carbon electrodes. Linear sweep voltammetry (LSV) under illumination (Fig. 6a) revealed that bare gCN and 5Mo-gCN exhibit negligible HER activity, confirming their limited intrinsic photocatalytic capability. After co-catalyst incorporation, it shows considerably higher HER activity where the lowest overpotential was obtained for 5CoMo-gCN. EIS measurements further supported these findings. The Nyquist plots (Fig. 6b) showed that while the high-frequency resistance (HFR) remained relatively constant across all samples (~5–8 Ω), the charge transfer resistance (R_{ct}) obtained from fitting the equivalent circuit (Fig. S7) varied considerably (Table S4). Notably, 5CoMo-gCN exhibited the lowest R_{ct} (26.5 Ω), followed by 5Co-gCN (194.8 Ω), indicating enhanced interfacial charge transport and faster surface redox processes in samples containing Co. However, the lowest R_{ct} in 5CoMo-gCN can be attributed to the synergistic effect of Co and Mo, which facilitates efficient separation and transfer of photo-generated charge carriers. The improved kinetics likely originate from better electron injection across the catalyst/electrolyte interface. Mott–Schottky (M−S) plot (Fig. 6c) showed positive slopes for gCN and 5CoMo-gCN, confirming their n-type semiconducting behaviour. The donor charge density was calculated using the Mott-Schottky equation [75], yielding a value of 2.2012×10^{19} cm^{-3} for gCN and 6.6052×10^{19} cm^{-3} for 5CoMo-gCN. The higher electron density in 5CoMo-gCN highlights that the co-catalysts enhance charge accumulation by acting as electron traps, increasing the availability of photogenerated electrons for HER. Based on the calculated V_{FB}, both gCN and 5CoMo-gCN show a V_{FB} of −1.2 V (vs RHE), matching well with the reported values for gCN NS [76]. This suggests that the dual-metal co-catalyst does not affect the energy levels of the gCN and its role is confined to surface trapping of photo-generated electrons that are eventually utilized for the HER.

The effect of co-catalyst integration on charge recombination was studied through steady-state photoluminescence (PL) measurements. The steady-state PL spectra (Fig. 6d) was obtained after optically exciting the catalysts with photons of wavelength 370 nm. The intensity of the PL spectra is directly related to the radiative recombination process and decrease in PL signal indicates improved charge separation [77]. Pristine gCN NS showed the highest PL intensity, consistent with rapid charge recombination and poor photocatalytic efficiency. Upon incremental loading of the CoMo co-catalyst, PL intensity progressively decreased, reaching a minimum and stabilizing at nominal 5 wt% (5CoMo-gCN), corresponding to actual 2.92 wt% of Co and Mo with the real Co:Mo ratio of 5.5. This suggests that the co-catalyst effectively extracts photo-generated charges from the gCN matrix, suppressing recombination via interfacial electron transfer. At higher loading levels, such as in 11CoMo-gCN, the PL intensity further decreased, implying enhanced electron trapping at the co-catalyst surface. However, this does not translate to improved performance due to the concurrent "shading/shielding effect", where excessive co-catalyst coverage limits light absorption by the underlying gCN layer [23,78]. As previously discussed, such overloading compromises photocatalytic activity despite better recombination suppression. 5Co-gCN also shows very low PL intensity while 5Mo-gCN shows very high intensity, impressing upon the

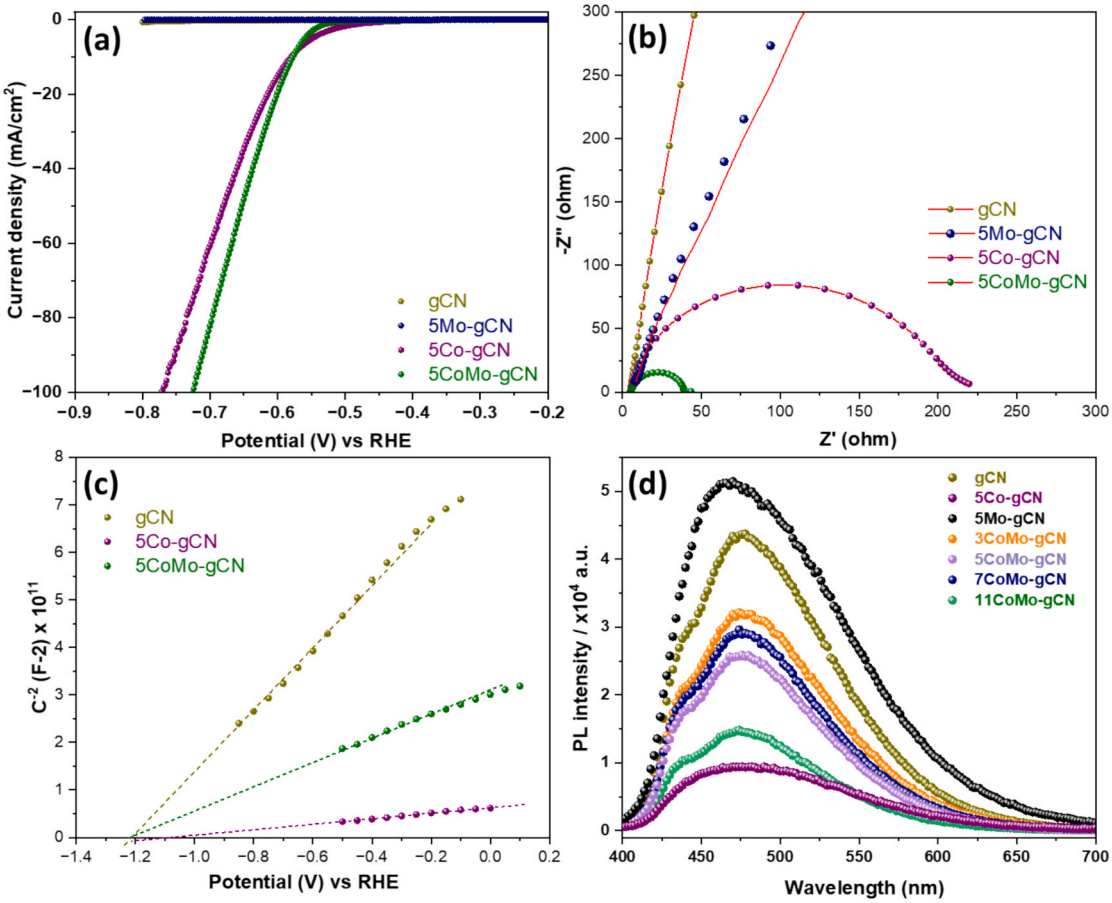

Fig. 6. (a) Linear sweep voltammetry and (b) Nyquist plots obtained from EIS for gCN, 5Mo-gCN, 5Co-gCN and 5CoMo-gCN; (c) Mott-Schottky plots for gCN, 5Co-gCN and 5CoMo-gCN; (d) Photoluminescence spectra for bare gCN and CoMo-gCN composites.

fact that Co sites are the ones responsible for electron trapping. Average charge carrier lifetimes were calculated from time-resolved photoluminescence (TRPL) measurements where the data was best fit using 3 exponential functions, among which fast (τ_1 and τ_2) and slow (τ_3) processes could be identified (Table S5). Bare gCN and 5Mo-gCN show slightly higher average lifetimes (14.1–14.3 ns) compared to the co-catalyst loaded composites (13.1–13.5 ns). This reduction of the lifetime between gCN and active Co-containing co-catalysts (drop from 14.3 ns to 13.5–13.1 ns range) is associated with the drop in both slow (from 39.8 ns to 37–38 ns rage) and fast (from 1.63 ns to 1.41–1.47 ns range and from 7.12 ns to 6.47–6.63 ns range) components. This implies a 7.5% drop in the average lifetime, but 13% drop in τ_1, 9% drop in τ_2 and 6% drop in τ_3, suggesting that the fastest component (τ_1) is affected most. Based on this, it is suggested that the interfacial charge transfer is the prime component that gets optimized in the system with the presence of the Co-containing co-catalyst. The smaller average lifetimes indicate that the photo-generated charges are short-lived as they may get trapped at the co-catalyst sites, making them available for redox reactions.

3.3. Post HER investigations

To understand the modifications in the material after photocatalytic testing, the sample was collected after 7 cycles of HER and analyzed using STEM and XPS while the remaining solution was analyzed with TXRF. In powder samples, the nano-sized particles that were observed on the surface of pristine samples (Fig. 3a) were not present after HER testing. However, STEM-HAADF image showed the presence of a large number of tiny bright spots on the surface of the gCN nanosheets (Fig. 7a). These bright spots are reminiscent of single metal atoms dispersed all over the gCN surface, which is also indicated from their average (apparent) sizes (Fig. 7b). EDS spectrum recorded over this dense region of single atoms confirm the presence of Co (Cu signal arises from the TEM grid). The Mo signal was not detected by EDS in the post-HER samples but Mo was found excessively in the solution, as detected with TXRF (Table S6). XPS data recorded for the post-HER sample gives C 1s and N 1s spectra similar to that observed in pristine samples, implying no significant change in gCN nanosheets during HER. However, the peak intensity corresponding to Co 2p and Mo 3d states was drastically diminished (Fig. 7d and 7g), which might be due to the decreased size (and density) of the co-catalysts. However, the confirmed presence of Co on gCN surface from STEM and XPS suggest that not all Co dissolved during HER or if it happened then there must be a re-deposition of Co in the form of single-atoms. Such dissolution/re-deposition phenomenon are reported for other metal catalysts in different applications [79–81]. The change in local environment of Co single atoms could be precisely investigated using in-situ XAS that will complement the current results. However, such studies are beyond the scope of this article. Based on the evidences from XPS, STEM and EDS, we propose that CoMo nanoparticles disintegrate during HER, where Co atoms re-deposit in the form of single-atom co-catalysts and remain well embedded into the gC_3N_4 framework, maintaining the structural integrity of the active Co component. This explains the consistent repeatability of the HER activity during successive cycling of the photocatalyst (Fig. 5b). The poor interaction between gCN and Mo atoms was already observed during synthesis where Mo deposition was not possible without Co mediation (Scheme 1). This suggests that the weakly adsorbed Mo species are most prone to dissolution during the reaction and explains their absence in the post-HER sample. We believe that Mo may serve the initial purpose of forming surface hydrides, which activates the catalyst surface for HER and then dissolves during HER.

3.4. Computational studies

To better understand the HER mechanism over the CoMo-gCN composite and elucidate the electronic interaction between Co and Mo atoms, DFT studies were performed by modeling a supercell of gCN layer (2x2x1) containing a Co cluster (Co-gCN) and a CoMo cluster (CoMo-gCN). During structural optimization of Co-gCN, it was observed that the void region in gCN layer offers energetic stability compared to the web for Co_{13} cluster. The Co_{13} cluster directly bonds with the edge nitrogen atoms within the g-CN void, which causes a corrugation of g-CN planar geometry. This corrugation also explains the delamination of gCN layers observed experimentally after co-catalyst loading. The energetic preference for the void and the cluster's tendency to directly bind with edge nitrogen are attributed to the inherent nature of the active edge nitrogen atoms, particularly their lone pair electrons.

To identify the favorable adsorption site in Co-gCN, a hydrogen atom was adsorbed over a surface Co atom. Upon optimization, it migrates over to a Co-Co bond (Co^1-Co^2), identifying the Co-Co bond as the active adsorption site. The change in Gibb's free energy (ΔG_{H^*}) and adsorption energy ΔE_H for hydrogen binding over the Co^1-Co^2 bond was found to be approximately −0.273 eV and −0.513 eV, respectively. For the CoMo-gCN structure, HER activity was investigated at different sites, namely

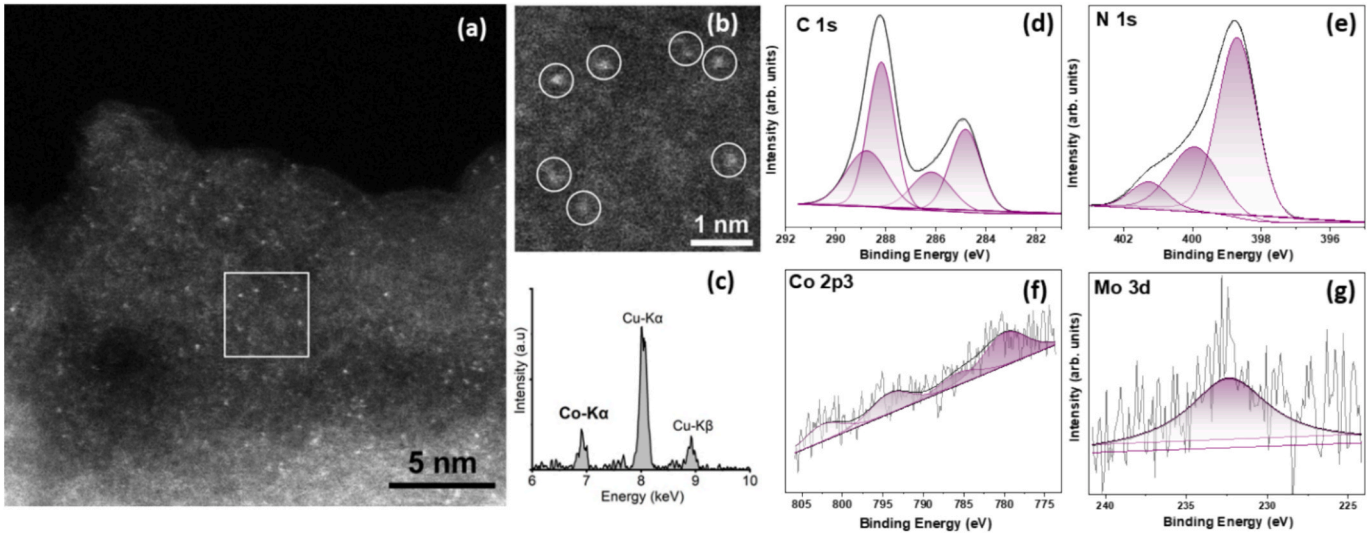

Fig. 7. (a) High-magnification STEM-HAADF image of 5CoMo-gCN recovered after photocatalytic HER cycles; (b) detail from (a) showing the presence of single-atoms with brighter contrast (higher Z) marked in white circles; (c) EDS spectrum from the region shown in (a); High-resolution XPS spectra for (d) C 1s, (e) N 1s and (f) Co 2p and (g) Mo 3d states in 5CoMo-gCN after photocatalytic HER cycles.

over surface Mo atom (Mo^S), Co^1, Co^1-Mo^S bond, and Co^1-Co^2 bond (Fig. 8a). The introduction of Mo significantly modulates the charge distribution of the neighboring environment, leading to stronger hydrogen binding. ΔG_{H^*} values of approximately −0.602 eV and −0.585 eV and ΔE_H values of −0.842 eV and −0.825 eV were calculated for hydrogen adsorption over Mo^S and Co^1-Mo^S bond, respectively. Further, hydrogen adsorption over the Co^1-Co^2 bond in CoMo-gCN resulted in stronger binding compared to that in Co-gCN, with a ΔG_{H^*} of about −0.322 eV (Fig. 8c), which is attributed to the charge modulation induced by Mo inclusion.

The stronger hydrogen binding at Mo^S and Co^1-Mo^S bond sites leads to a reformation of the electrolyte/catalyst interface through surface reconstruction of the CoMo cluster, where H-coverage builds up until an equilibrium is achieved with the electrolyte. This surface reconstruction can result in the formation of metal hydrides during in-situ reactions, consistent with various reported studies [72,73]. To simulate the effect of hydrogen coverage, the Mo^S atom was saturated with hydrogen adsorption (Fig. 8b) and the resulting structure is denoted as $CoMo^{(H)}$-gCN. The HER activity over the neighboring active Co^1-Co^2 bond gets significantly enhanced due to this saturation, with a much smaller ΔG_{H^*} of approximately 0.068 eV, highlighting its higher favorability for HER (Fig. 8c).

Based on Löwdin charge transfer (Table S7), the introduction of Mo in CoMo-gCN primarily alters the electronic structure of neighboring Co atoms. In this configuration, both the surface molybdenum (Mo^S) and central molybdenum (Mo^C) atoms act as significant electron donors, exhibiting positive charge transfer values (0.6031 e^- for Mo^S and 0.7081 e^- for Mo^C). This electron donation leads to an increased electron density on Co sites, as indicated by negative charge transfer values for Co^1 (−0.2169 e^-) and Co^2 (−0.1183 e^-). The resulting ΔG_{H^*} over Co^1-Co^2 bond in CoMo-gCN is −0.322 eV, which suggests an unfavorably strong binding of hydrogen, hindering desorption during HER. The enrichment of electron density is also visualized by the ELF (Fig. S9a-b), displaying increased metallic character of the bonds. In case of $CoMo^{(H)}$-gCN system, Mo^S (0.7603 e^-) and Mo^C (0.7687 e^-) continue to act as electron donors, with Mo^S showing an even higher degree of electron loss compared to CoMo-gCN (Table S7). Notably, the pre-adsorbed hydrogen atom saturating the Mo surface (H^{SAT}) exhibits a significant negative charge transfer of −0.1843 e^-, acting as an electron sink. This indicates that Mo^S now directly donates electrons to H^{SAT}. In this process, Co^1 also gains charges (−0.2858 e^-) with almost no changes in Co^2. The overall total charges are mainly accepted by H^{SAT}, saturating the Mo atoms, eventually showing good HER activity with a ΔG_{H^*} of approximately 0.068 eV due to optimized binding of hydrogen over the Co^1-Co^2 bond. This saturation of the Mo^S by H^{SAT} also leads to a reduction in metallicity between Co^1-Co^2 bond (Fig. S9c). When comparing the electron charge transfer over the hydrogen atom undergoing HER (H^{HER}), very small negative charge is transferred in unsaturated CoMo-gCN, maintaining a near-neutral state. Conversely, in $CoMo^{(H)}$-gCN, the pre-adsorbed H^{SAT} (−0.2014 e^-) continues to draw electrons, leading to back-propagation of charges from Co^1-Co^2, enhancing the charge-neutral state of the H^{HER} (−0.0049 e^-), leading to more optimized binding.

3.5. Discussion of photocatalytic mechanism

Based on the various investigations, we propose a possible mechanism for the photocatalytic HER on 5CoMo-gCN photocatalyst (Fig. 9). The generation of photo-electrons in gC_3N_4 and their migration to the co-catalyst sites (acting as surface traps) is a routine pathway that we observe in this case as well. However, as the co-catalyst comprises of dual-metal atoms, the redox mechanism is different, where Co acts as the primary catalytic center, while Mo (as Mo oxide) enhances the adsorption and stabilization of H* intermediates (confirmed through DFT studies), through electronic modulation and transient hydride formation, accelerating the overall HER kinetics. The bonding between Co and Mo was confirmed through XAS and interaction between them was verified through XPS and DFT studies. It is notable that initially Co exists in oxide form but is photo-reduced during HER and follows the speculated dissolution/re-deposition pathway to form metallic single-atom co-catalysts, which are much more active for HER [61,62]. The synergistic roles played by Co and Mo justifies the higher HER rates in 5CoMo-gCN compared to 5Co-gCN containing a single metal. Importantly, absorption spectra and Mott-Schottky analyses confirm that the incorporation of CoMo does not significantly alter the bandgap or V_{FB} of g-C_3N_4, suggesting that the co-catalyst operates via surface-mediated electron trapping rather than bulk electronic restructuring. EIS and LSV data

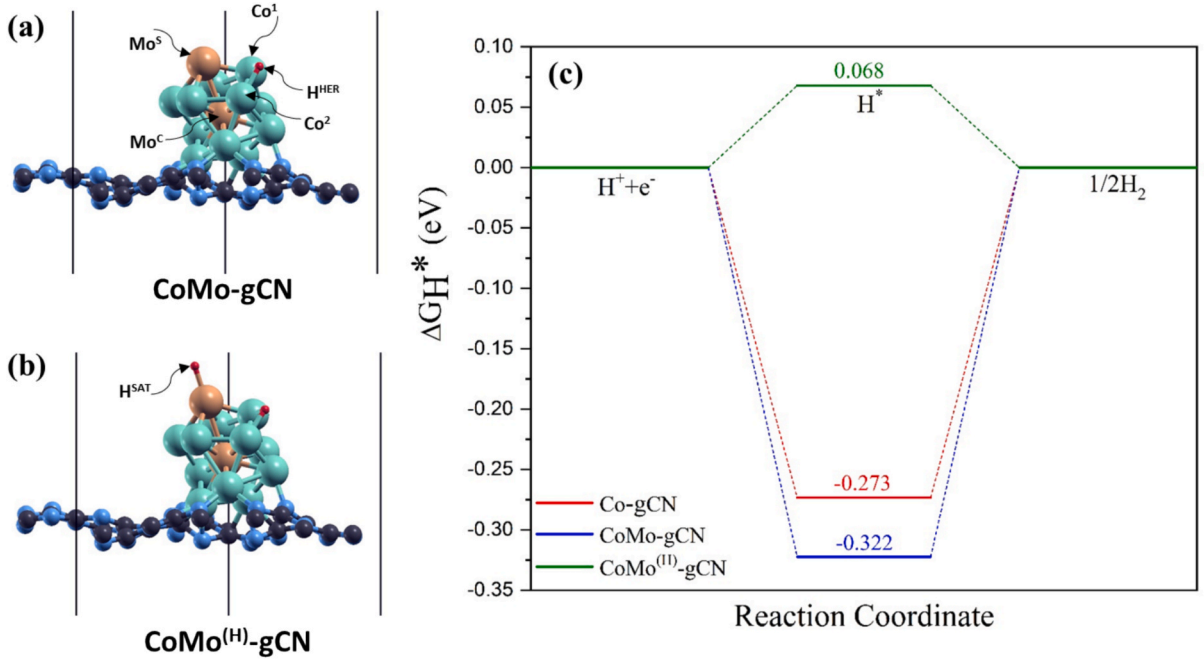

Fig. 8. Side view of optimized (a) CoMo-gCN and (b) $CoMo^{(H)}$-gCN; (c) Gibbs free energy versus reaction coordinate plot for HER at potential U = 0 for Co-gCN, CoMo-gCN, and $CoMo^{(H)}$-gCN.

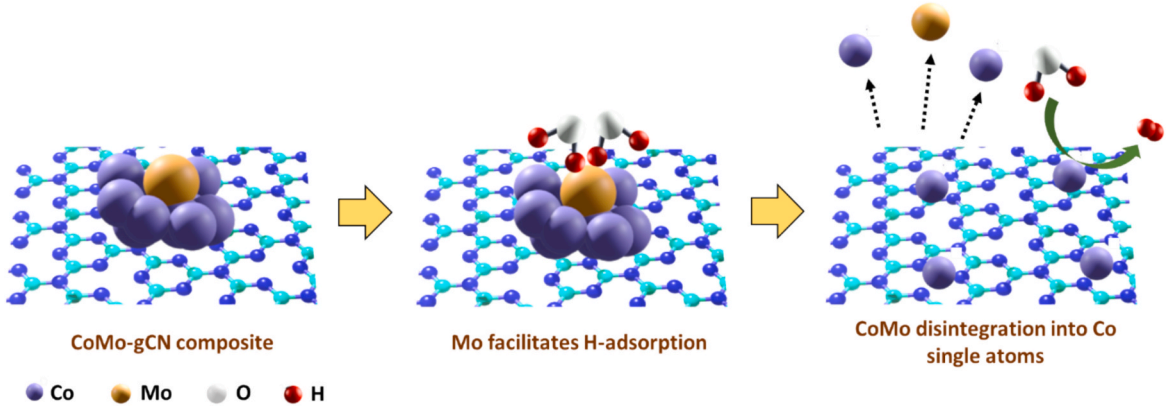

Fig. 9. Scheme representing the co-catalyst transformation during photocatalytic HER.

further corroborate this by showing decreased charge transfer resistance and overpotential upon CoMo loading, indicative of enhanced interfacial charge kinetics. DFT calculations show that Mo atoms in CoMo-gCN act as effective electron donors, leading to an increased electron density on the adjacent Co sites. This electronic enrichment, confirmed by Löwdin charge transfer and ELF analyses, initially results in stronger hydrogen binding, characterized by more negative ΔG_{H^*} and potentially hindering efficient hydrogen desorption. However, the electron-donating nature of Mo facilitates a rapid build-up of hydrogen coverage on the catalyst surface, particularly by capturing hydrogen atoms at Mo and Co-Mo active sites during the initial reaction phase. This increased hydrogen coverage triggers a vital surface reconstruction of the CoMo cluster, which reconfigures the electrolyte/catalyst interface, leading to the formation of metal hydrides. The saturation of surface Mo sites with hydrides effectively "dysfunctions" the electron donation to the active Co sites, optimizing the charge environment and leads to a significantly improved hydrogen binding energy (ΔG_{H^*} of approximately 0.06 eV), which is manifested in higher HER rates. Overall, the mechanism highlights the pivotal role of dual-metal CoMo co-catalysts in enhancing the spatial separation of photoinduced charge carriers and promoting interfacial redox reactions, thereby enabling efficient HER under visible light irradiation.

4. Conclusion

In this work, a dual-metal co-catalyst (CoMo) integrated onto exfoliated gCN nanosheets was successfully developed for efficient photocatalytic hydrogen evolution under visible light irradiation. Detailed structural, morphological, and spectroscopic analyses confirm the uniform dispersion of ultra-small CoMo nanoclusters (<5 nm) on the gCN surface and reveal a strong electronic interaction between the co-catalyst and the host semiconductor. XAS and XPS results verify the formation of Co–Mo co-ordination environments and indicate charge redistribution at the metal–support interface. Optimization studies reveal that a nominal Co:Mo ratio of 0.7:0.3 (actual Co:Mo = 5.5:1) with a nominal 5 wt% (actual 2.92 wt%) loading delivers the highest HER performance, outperforming single-metal counterparts and bare gCN by significant margins. Electrochemical and spectroscopic investigations demonstrate enhanced charge separation, reduced recombination, and improved interfacial electron transfer in the presence of the CoMo co-catalyst. Crucially, optical and Mott-Schottky analyses show that the band structure of g-CN remains intact, indicating a surface-limited role for the co-catalyst. The proposed mechanism highlights the synergistic contributions of Co and Mo, where Co serves as the primary active site for proton reduction, while Mo facilitates H* stabilization. The role of Mo was validated through computational studies where Mo was found to act as the electron donor that not only modulates electronic density of neighboring Co atoms but also facilitates hydrogen coverage over the surface, leading to energetically favorable conditions for HER. Post-HER measurements show disintegration of CoMo nanoparticles into Co single-atom sites that remain embedded into the gCN sheets. Consequently, the optimized 5CoMo-gCN composite showed commendable stability under dynamic operating conditions for over 13 h, suggesting its applicability for longer hours of operation at possibly larger scales. These findings establish CoMo as a promising non-noble alternative for noble-metal co-catalysts that are typically used with gCN for solar hydrogen production. The study offers a compelling case for the research and development of similar dual-metal co-catalyst systems aimed at further enhancing the photocatalytic performances of not only gCN NS but other photo-absorber systems as well.

CRediT authorship contribution statement

Suraj Gupta: Writing – original draft, Visualization, Validation, Supervision, Methodology, Investigation, Formal analysis, Data curation, Conceptualization. **Samar Batool:** Validation, Methodology, Investigation, Formal analysis. **Marjeta Maček Kržmanc:** Writing – review & editing, Methodology, Investigation, Funding acquisition, Formal analysis. **Nina Daneu:** Writing – review & editing, Visualization, Methodology, Investigation, Formal analysis, Data curation. **Joyal Johny:** Visualization, Methodology, Formal analysis. **Rohan Arya:** Software, Methodology, Investigation, Formal analysis, Data curation. **Kishan H. Mali:** Visualization, Validation, Software, Methodology, Investigation, Formal analysis, Data curation. **Alpa Dashora:** Writing – review & editing, Software, Resources, Methodology, Investigation, Funding acquisition, Formal analysis, Data curation. **Harishchandra Singh:** Methodology, Investigation, Formal analysis. **A.K. Yadav:** Writing – review & editing, Methodology, Investigation, Formal analysis, Data curation. **Nainesh Patel:** Writing – review & editing, Methodology, Investigation, Funding acquisition, Formal analysis, Data curation. **Pablo Ayala:** Methodology, Investigation, Formal analysis, Data curation. **Matjaž Spreitzer:** Resources, Project administration, Methodology, Funding acquisition. **Dominik Eder:** Writing – review & editing, Supervision, Resources, Investigation, Funding acquisition, Formal analysis. **Alexey Cherevan:** Writing – review & editing, Supervision, Investigation, Funding acquisition, Formal analysis, Data curation.

Declaration of competing interest

The authors declare that they have no known competing financial interests or personal relationships that could have appeared to influence the work reported in this paper.

Acknowledgements

S. Gupta, M. Maček Kržmanc, N. Daneu and M. Spreitzer acknowledge the Ministry of Higher Education, Science and Innovation from Slovenia to provide support for M-ERA.NET project HetCat (No. 10382) Contract No. C3360-23-252003, Slovenian Research and Innovation Agency for financing of the research projects (P2–0091, J2-50055) and the bilateral IJS-CNR project. K.H. Mali and A. Dashora are thankful for the financial support provided by SERB, New Delhi under scheme SUR/2022/002252. A. Dashora is grateful to UGC, New Delhi for the Assistant Professorship under the Faculty Recharge Program. H. Singh acknowledges Prof. Marko Huttula, Strategic Research Council within the Research Council of Finland decision 358422 and JustH2Transit, the EU/Interreg Aurora/Sustainable Hydrogen Project, and ANRF, Department of Science and Technology, India, through the Ramanujan Faculty Award (RJF/2023/000058) for financial support. We are thankful to Damjan Vengust for assisting with TEM measurements and Stephen Myakala for assisting with HER experiments.

Appendix A. Supplementary data

Supplementary data to this article can be found online at https://doi.org/10.1016/j.fuel.2026.140103.

Data availability

Data will be made available on request.

References

[1] Fu H, Wu Y, Guo Y, Sakurai T, Zhang Q, Liu Y, et al. A scalable solar-driven photocatalytic system for separated H2 and O2 production from water. Nat Commun 2025;16:990. https://doi.org/10.1038/s41467-025-56314-x.
[2] Segev G, Kibsgaard J, Hahn C, Xu ZJ, Deutsch TG, Xiang C, et al. The 2022 solar fuels roadmap. J Phys D Appl Phys 2022;55:323003.
[3] Fujishima A, Honda K. Electrochemical photolysis of water at a semiconductor electrode. Nature 1972;238:37.
[4] Kudo A, Miseki Y. Heterogeneous photocatalyst materials for water splitting. Chem Soc Rev 2009;38:253–78.
[5] Wang Q, Hisatomi T, Jia Q, Tokudome H, Zhong M, Wang C, et al. Scalable water splitting on particulate photocatalyst sheets with a solar-to-hydrogen energy conversion efficiency exceeding 1%. Nat Mater 2016;15:611–5. https://doi.org/10.1038/nmat4589.
[6] Chen S, Li C, Domen K, Zhang F. Particulate metal chalcogenides for photocatalytic Z-scheme overall water splitting. Joule 2023;7:2445–67. https://doi.org/10.1016/j.joule.2023.10.004.
[7] Moniz SJA, Shevlin SA, Martin DJ, Guo Z-X, Tang J. Visible-light driven heterojunction photocatalysts for water splitting – a critical review. Energy Environ Sci 2015;8:731–59. https://doi.org/10.1039/C4EE03271C.
[8] Wang H, Zhang L, Chen Z, Hu J, Li S, Wang Z, et al. Semiconductor heterojunction photocatalysts: design, construction, and photocatalytic performances. Chem Soc Rev 2014;43:5234–44. https://doi.org/10.1039/C4CS00126E.
[9] Yu H, Dai M, Zhang J, Chen W, Jin Q, Wang S, et al. Interface engineering in 2D/2D heterogeneous photocatalysts. Small 2023;19:2205767. https://doi.org/10.1002/smll.202205767.
[10] Zhao Y, Zhang S, Shi R, Waterhouse GIN, Tang J, Zhang T. Two-dimensional photocatalyst design: a critical review of recent experimental and computational advances. Mater Today 2020;34:78–91. https://doi.org/10.1016/j.mattod.2019.10.022.
[11] Nasir MS, Yang G, Ayub I, Wang S, Wang L, Wang X, et al. Recent development in graphitic carbon nitride based photocatalysis for hydrogen generation. Appl Catal B 2019;257:117855. https://doi.org/10.1016/j.apcatb.2019.117855.
[12] Ding X, Wang Q, Liu H, Wang J, Yan P, Chen H, et al. Research progress of graphitic carbon nitride in photocatalytic hydrogen evolution. Int J Hydrogen Energy 2025;187:152004. https://doi.org/10.1016/j.ijhydene.2025.152004.
[13] Nagar OP, Chouhan N. Non-metal doped graphitic carbon nitride (g-C3N4): prospects and review on hydrogen generation via water splitting. Int J Hydrogen Energy 2024;96:533–65. https://doi.org/10.1016/j.ijhydene.2024.10.415.
[14] Lau VW, Lotsch BV. A tour-guide through carbon nitride-land: structure-and dimensionality-dependent properties for photo (electro) chemical energy conversion and storage. Adv Energy Mater 2022;12:2101078.
[15] Fan Y, Lei L, Cao J, Wang W, Fan H. Benzene ring engineering of graphitic carbon nitride for enhanced photocatalytic dye degradation and hydrogen production from water splitting. ChemSusChem 2025;18. https://doi.org/10.1002/cssc.202500462.
[16] Humayun M, Ullah H, Tahir AA, Bin Mohd Yusoff AR, Mat Teridi MA, Nazeeruddin MK, et al. An overview of the recent progress in polymeric carbon nitride based photocatalysis. Chem Rec 2021;21:1811–44.
[17] Rahman MZ, Mullins CB. Understanding charge transport in carbon nitride for enhanced photocatalytic solar fuel production. Acc Chem Res 2018;52:248–57.
[18] Zhang G, Li G, Lan Z-A, Lin L, Savateev A, Heil T, et al. Optimizing optical absorption, exciton dissociation, and charge transfer of a polymeric carbon nitride with ultrahigh solar hydrogen production activity. Angew Chem Int Ed 2017;56:13445–9. https://doi.org/10.1002/anie.201706870.
[19] Ma D, Zhang Z, Zou Y, Chen J, Shi J-W. The progress of g-C3N4 in photocatalytic H2 evolution: from fabrication to modification. Coord Chem Rev 2024;500:215489. https://doi.org/10.1016/j.ccr.2023.215489.
[20] Wen J, Xie J, Chen X, Li X. A review on g-C3N4-based photocatalysts. Appl Surf Sci 2017;391:72–123.
[21] Zhu Q, Xu Z, Qiu B, Xing M, Zhang J. Emerging cocatalysts on g-C3N4 for photocatalytic hydrogen evolution. Small 2021;17:2101070. https://doi.org/10.1002/smll.202101070.
[22] Kadlag AG, Jawale NS, Tambe AB, Umarji GG, Kanade CK, Lonkar SP, et al. Coherent design of NiO/g-C3N4 based nano heterojunction photocatalyst for hydrogen generation. Int J Hydrogen Energy 2026;197:152301. https://doi.org/10.1016/j.ijhydene.2025.152301.
[23] Zhu Y, Xu Y, Hou Y, Ding Z, Wang X. Cobalt sulfide modified graphitic carbon nitride semiconductor for solar hydrogen production. Int J Hydrogen Energy 2014;39:11873–9. https://doi.org/10.1016/j.ijhydene.2014.06.025.
[24] Gupta S, Prapaitrakool C, Bhagat BR, Yeh C-L, Dashora A, Sirisuk A, et al. Promoting photocatalytic hydrogen evolution rates in layered graphitic carbon nitride through integrated non-noble CoB co-catalyst. Int J Hydrogen Energy 2024;60:1288–98. https://doi.org/10.1016/j.ijhydene.2024.02.261.
[25] Zhao N, Kong L, Dong Y, Wang G, Wu X, Jiang P. Insight into the crucial factors for photochemical deposition of cobalt cocatalysts on g-C3N4 photocatalysts. ACS Appl Mater Interfaces 2018;10:9522–31. https://doi.org/10.1021/acsami.8b01590.
[26] Ge L, Han C, Xiao X, Guo L. In situ synthesis of cobalt–phosphate (Co–Pi) modified g-C3N4 photocatalysts with enhanced photocatalytic activities. Appl Catal B 2013;142–143:414–22. https://doi.org/10.1016/j.apcatb.2013.05.051.
[27] Sun C, Zhang H, Liu H, Zheng X, Zou W, Dong L, et al. Enhanced activity of visible-light photocatalytic H2 evolution of sulfur-doped g-C3N4 photocatalyst via nanoparticle metal Ni as cocatalyst. Appl Catal B 2018;235:66–74. https://doi.org/10.1016/j.apcatb.2018.04.050.
[28] Liu J, Jia Q, Long J, Wang X, Gao Z, Gu Q. Amorphous NiO as co-catalyst for enhanced visible-light-driven hydrogen generation over g-C3N4 photocatalyst. Appl Catal B 2018;222:35–43. https://doi.org/10.1016/j.apcatb.2017.09.073.
[29] Zeng D, Zhou T, Ong W-J, Wu M, Duan X, Xu W, et al. Sub-5 nm ultra-fine FeP nanodots as efficient co-catalysts modified porous g-C3N4 for precious-metal-free photocatalytic hydrogen evolution under visible light. ACS Appl Mater Interf 2019;11:5651–60. https://doi.org/10.1021/acsami.8b20958.
[30] Wang W, An T, Li G, Xia D, Zhao H, Yu JC, et al. Earth-abundant Ni2P/g-C3N4 lamellar nanohydrids for enhanced photocatalytic hydrogen evolution and bacterial inactivation under visible light irradiation. Appl Catal B 2017;217:570–80. https://doi.org/10.1016/j.apcatb.2017.06.027.
[31] Wei R, Tang N, Jiang L, Yang J, Guo J, Yuan X, et al. Bimetallic nanoparticles meet polymeric carbon nitride: Fabrications, catalytic applications and perspectives. Coord Chem Rev 2022;462:214500. https://doi.org/10.1016/j.ccr.2022.214500.
[32] Chen S, Hau Ng Y, Liao J, Gao Q, Yang S, Peng F, et al. FeCo alloy@N-doped graphitized carbon as an efficient cocatalyst for enhanced photocatalytic H2 evolution by inducing accelerated charge transfer. J Energy Chem 2021;52:92–101. https://doi.org/10.1016/j.jechem.2020.04.040.
[33] Gao Y, Chen F, Chen Z, Shi H. NixCo1-xS as an effective noble metal-free cocatalyst for enhanced photocatalytic activity of g-C3N4. J Mater Sci Technol 2020;56:227–35. https://doi.org/10.1016/j.jmst.2020.02.050.
[34] Han X, Xu D, An L, Hou C, Li Y, Zhang Q, et al. Ni-Mo nanoparticles as co-catalyst for drastically enhanced photocatalytic hydrogen production activity over g-C3N4. Appl Catal B 2019;243:136–44. https://doi.org/10.1016/j.apcatb.2018.10.003.
[35] Jin Z, Zhang L. Performance of Ni-Cu bimetallic co-catalyst g-C3N4 nanosheets for improving hydrogen evolution. J Mater Sci Technol 2020;49:144–56.
[36] Chen M, Zhou X, Luo J, Zhou X, Ge Y. Boosting photocatalytic hydrogen evolution of g-C3N4 via enhancing its interfacial redox activity and charge separation with Mo-doped CoSx. Int J Hydrogen Energy 2022;47:35723–36. https://doi.org/10.1016/j.ijhydene.2022.08.158.
[37] Zhou X, Luo J, Jin B, Wu Z, Yang S, Zhang S, et al. Sustainable synthesis of low-cost nitrogen-doped-carbon coated Co3W3C@g-C3N4 composite photocatalyst for efficient hydrogen evolution. Chem Eng J 2021;426:131208. https://doi.org/10.1016/j.cej.2021.131208.
[38] Gupta S, Patel N, Fernandes R, Hanchate S, Miotello A, Kothari DC. Co-Mo-B nanoparticles as a non-precious and efficient bifunctional electrocatalyst for hydrogen and oxygen evolution. Electrochim Acta 2017;232:64–71. https://doi.org/10.1016/j.electacta.2017.02.100.
[39] Sun Z, Hao S, Ji X, Zheng X, Xie J, Li X, et al. Efficient alkaline hydrogen evolution electrocatalysis enabled by an amorphous Co–Mo–B film. Dalton Trans 2018;47:7640–3. https://doi.org/10.1039/C8DT01296B.
[40] Zhao X, Yin F, He X, Chen B, Li G. Efficient overall water splitting over a Mo(IV)-doped Co3O4/NC electrocatalyst. Int J Hydrogen Energy 2021;46:20905–18. https://doi.org/10.1016/j.ijhydene.2021.03.187.
[41] Meena PL, Poswal K, Surela AK, Saini JK. Synthesis of graphitic carbon nitride/zinc oxide (g-C3N4/ZnO) hybrid nanostructures and investigation of the effect of ZnO on the photodegradation activity of g-C3N4 against the brilliant cresyl blue (BCB)

dye under visible light irradiation. Adv Compos Hybrid Mater 2022;6:16. https://doi.org/10.1007/s42114-022-00577-1.
[42] Li N, Tian Y, Zhao J, Zhang J, Zuo W, Kong L, et al. Z-scheme 2D/3D g-C3N4@ZnO with enhanced photocatalytic activity for cephalexin oxidation under solar light. Chem Eng J 2018;352:412–22. https://doi.org/10.1016/j.cej.2018.07.038.
[43] Ciatto G, Chu MH, Fontaine P, Aubert N, Renevier H, Deschanvres JL. SIRIUS: a new beamline for in situ X-ray diffraction and spectroscopy studies of advanced materials and nanostructures at the SOLEIL Synchrotron. Thin Solid Films 2016;617:48–54.
[44] Jones RG. X-ray absorption: Principles, applications, techniques of EXAFS, SEXAFS, and XANES: Edited by DC Koningsberger and R. Prins. Pp. 673. Wiley, Chichester. 1988.£ 77.50 1988.
[45] Newville M, Ravel B, Haskel D, Rehr JJ, Stern EA, Yacoby Y. Analysis of multiple-scattering XAFS data using theoretical standards. Phys B Condens Matter 1995;208:154–6.
[46] Batool S, Nandan SP, Myakala SN, Rajagopal A, Schubert JS, Ayala P, et al. Surface anchoring and active sites of [Mo3S13]2– clusters as co-catalysts for photocatalytic hydrogen evolution. ACS Catal 2022;12:6641–50. https://doi.org/10.1021/acscatal.2c00972.
[47] Giannozzi P, Baroni S, Bonini N, Calandra M, Car R, Cavazzoni C, et al. QUANTUM ESPRESSO: a modular and open-source software project for quantum simulations of materials. J Phys Condens Matter 2009;21:395502.
[48] Rodríguez-López JL, Aguilera-Granja F, Michaelian K, Vega A. Structure and magnetism of cobalt clusters. Phys Rev B 2003;67:174413.
[49] Rives S, Catherinot A, Dumas-Bouchiat F, Champeaux C, Videcoq A, Ferrando R. Growth of Co isolated clusters in the gas phase: experiment and molecular dynamics simulations. Phys Rev B—Condens Matter Mater Phys 2008;77:85407.
[50] Li Z, Gu B. Electronic-structure calculations of cobalt clusters. Phys Rev B 1993;47:13611.
[51] Bhagat BR, Dashora A. Understanding the synergistic effect of Co-loading and B-doping in g-C3N4 for enhanced photocatalytic activity for overall solar water splitting. Carbon N Y 2021;178:666–77.
[52] Perdew JP, Burke K, Ernzerhof M. Generalized gradient approximation made simple. Phys Rev Lett 1996;77:3865–8. https://doi.org/10.1103/PhysRevLett.77.3865.
[53] Grimme S, Antony J, Ehrlich S, Krieg H. A consistent and accurate ab initio parametrization of density functional dispersion correction (DFT-D) for the 94 elements H-Pu. J Chem Phys 2010;132.
[54] Nørskov JK, Bligaard T, Logadottir A, Kitchin JR, Chen JG, Pandelov S, et al. Trends in the exchange current for hydrogen evolution. J Electrochem Soc 2005;152:J23.
[55] Benedoue SA, Ndi JN, Ge M, Tian Z, Dantio Nguela CB, Tong H, et al. Controllable acid activation of sulfur-doped carbon nitride enables enhancement in photocatalytic indigo carmine degradation performance. ACS Sust Chem Eng 2024;12:16809–16. https://doi.org/10.1021/acssuschemeng.4c08021.
[56] Yadav A, Gupta S, Bhagat BR, Yadav M, Dashora A, Varma RS, et al. Unraveling the synergy between oxygen doping and embedding Fe nanoparticles in gC3N4 towards enhanced photocatalytic rates. Appl Surf Sci 2022;603:154404. https://doi.org/10.1016/j.apsusc.2022.154404.
[57] Dong F, Li Y, Wang Z, Ho W-K. Enhanced visible light photocatalytic activity and oxidation ability of porous graphene-like g-C3N4 nanosheets via thermal exfoliation. Appl Surf Sci 2015;358:393–403.
[58] Yang L, Liu X, Liu Z, Wang C, Liu G, Li Q, et al. Enhanced photocatalytic activity of g-C3N4 2D nanosheets through thermal exfoliation using dicyandiamide as precursor. Ceram Int 2018;44:20613–9. https://doi.org/10.1016/j.ceramint.2018.06.105.
[59] She X, Liu L, Ji H, Mo Z, Li Y, Huang L, et al. Template-free synthesis of 2D porous ultrathin nonmetal-doped g-C3N4 nanosheets with highly efficient photocatalytic H2 evolution from water under visible light. Appl Catal B 2016;187:144–53. https://doi.org/10.1016/J.APCATB.2015.12.046.
[60] Shembade UV, Shinde BT, Magadum MG, Wategaonkar SB, Chavan HV, Hatshan MR, et al. Development of Fe2O3 heterostructures anchored on 2D g-C3N4 composite electrode materials for supercapacitor activities. Solid State Sci 2025;164:107934. https://doi.org/10.1016/j.solidstatesciences.2025.107934.
[61] Chen C, Zhao J, Chen M, Hou W, Xu Y. In situ photodeposition of cobalt nanoparticles onto ZnIn2S4 enhancing H2 production under visible light. Mol Catal 2021;515:111930. https://doi.org/10.1016/j.mcat.2021.111930.
[62] Thabet SM, Abdelhamid HN, Ibrahim SA, El-Bery HM. Boosting photocatalytic water splitting of TiO2 using metal (Ru, Co, or Ni) co-catalysts for hydrogen generatio. Sci Rep 2024;14:10115. https://doi.org/10.1038/s41598-024-59608-0.
[63] Tsang C. Synthesis of lower-valent molybdenum oxides in aqueous solutions by reducing Na2MoO4 with NaBH4. J Mater Chem 1997;7:1003–6.
[64] Singh JA, Hoffman AS, Schumann J, Boubnov A, Asundi AS, Nathan SS, et al. Role of Co2C in ZnO-promoted co catalysts for alcohol synthesis from syngas. ChemCatChem 2019;11:799–809. https://doi.org/10.1002/cctc.201801724.
[65] Lu Z, Li C, Han J, Wang L, Wang S, Ni L, et al. Construction 0D/2D heterojunction by highly dispersed Ni2P QDs loaded on the ultrathin g-C3N4 surface towards superhigh photocatalytic and photoelectric performance. Appl Catal B 2018;237:919–26. https://doi.org/10.1016/j.apcatb.2018.06.062.
[66] Yang J, Liu H, Martens WN, Frost RL. Synthesis and characterization of cobalt hydroxide, cobalt oxyhydroxide, and cobalt oxide nanodiscs. J Phys Chem C 2009;114:111–9.
[67] Wang R-C, Lin Y-C, Chen H-C, Lin W-Y. Energy harvesting from g-C3N4 piezoelectric nanogenerators. Nano Energy 2021;83:105743. https://doi.org/10.1016/j.nanoen.2021.105743.
[68] Zhang X, Yan J, Zheng F, Zhao J, Lee LYS. Designing charge transfer route at the interface between WP nanoparticle and g-C3N4 for highly enhanced photocatalytic CO2 reduction reaction. Appl Catal B 2021;286:119879. https://doi.org/10.1016/j.apcatb.2021.119879.
[69] Thommes M, Kaneko K, Neimark AV, Olivier JP, Rodriguez-Reinoso F, Rouquerol J, et al. Physisorption of gases, with special reference to the evaluation of surface area and pore size distribution (IUPAC Technical Report) 2015;87:1051–69. https://doi.org/10.1515/pac-2014-1117.
[70] Liang J, Jiang Z, Wong PK, Lee C-S. Recent progress on carbon nitride and its hybrid photocatalysts for CO2 reduction. Sol RRL 2021;5:2000478. https://doi.org/10.1002/solr.202000478.
[71] Batool S, Schubert JS, Ayala P, Saito H, Sampaio MJ, Da Silva ES, et al. A thiomolybdate cluster for visible-light-driven hydrogen evolution: comparison of homogeneous and heterogeneous approaches. Sust Energy Fuels 2024;8:1225–35. https://doi.org/10.1039/D3SE01658G.
[72] Tran PD, Tran TV, Orio M, Torelli S, Truong QD, Nayuki K, et al. Coordination polymer structure and revisited hydrogen evolution catalytic mechanism for amorphous molybdenum sulfide. Nat Mater 2016;15:640–6. https://doi.org/10.1038/nmat4588.
[73] Huang Y, Nielsen RJ, Goddard WAIII, Soriaga MP. The reaction mechanism with free energy barriers for electrochemical dihydrogen evolution on MoS2. J Am Chem Soc 2015;137:6692–8. https://doi.org/10.1021/jacs.5b03329.
[74] Trasatti S. Work function, electronegativity, and electrochemical behaviour of metals: III. Electrolytic hydrogen evolution in acid solutions. J Electroanal Chem Interfacial Electrochem 1972;39:163–84.
[75] Karimi-Nazarabad M, Goharshadi EK, Mahdizadeh SJ. Efficient photoelectrocatalytic water oxidation by palladium doped g-C3N4 electrodeposited thin film. J Phys Chem C 2019;123:26106–15. https://doi.org/10.1021/acs.jpcc.9b07755.
[76] Liu C, Huang H, Cui W, Dong F, Zhang Y. Band structure engineering and efficient charge transport in oxygen substituted g-C3N4 for superior photocatalytic hydrogen evolution. Appl Catal B 2018;230:115–24. https://doi.org/10.1016/j.apcatb.2018.02.038.
[77] Zhang X, Matras-Postolek K, Yang P, Jiang SP. Pt clusters in carbon network to enhance photocatalytic CO2 and benzene conversion of WOx/g-C3N4 nanosheets. Carbon N Y 2023;214:118337. https://doi.org/10.1016/j.carbon.2023.118337.
[78] Ong W-J, Tan L-L, Chai S-P, Yong S-T. Graphene oxide as a structure-directing agent for the two-dimensional interface engineering of sandwich-like graphene–g-C3N4 hybrid nanostructures with enhanced visible-light photoreduction of CO2 to methane. Chem Commun 2015;51:858–61. https://doi.org/10.1039/C4CC08996K.
[79] Lutterman DA, Surendranath Y, Nocera DG. A self-healing oxygen-evolving catalyst. J Am Chem Soc 2009;131:3838–9. https://doi.org/10.1021/ja900023k.
[80] Vavra J, Shen T-H, Stoian D, Tileli V, Buonsanti R. Real-time monitoring reveals dissolution/redeposition mechanism in copper nanocatalysts during the initial stages of the CO2 reduction reaction. Angew Chem Int Ed 2021;60:1347–54. https://doi.org/10.1002/anie.202011137.
[81] Zhang Y, Hu A, Xia D, Hwang S, Sainio S, Nordlund D, et al. Operando characterization and regulation of metal dissolution and redeposition dynamics near battery electrode surface. Nat Nanotechnol 2023;18:790–7. https://doi.org/10.1038/s41565-023-01367-6.